ADVANCED FUNCTIONAL MATERIALS
www.afm-journal.de

The Conformal, High-Density SpineWrap Microelectrode Array for Focal Stimulation and Selective Muscle Recruitment

*Samantha M. Russman, Rhea Montgomery-Walsh, Ritwik Vatsyayan, Hoi Sang U, Luis D. Diaz-Aguilar, Eric Y. Chang, Qingbo Tang, Keundong Lee, Tony L. Yaksh, Sharona Ben-Haim, Joseph Ciacci, and Shadi A. Dayeh**

Epidural electrical stimulation (EES) of the spinal cord is widely applied for pain management and as a possible route to functional restoration after spinal cord injury. Currently, EES employs bulky, nonconformal paddle arrays with low channel counts. This limits stimulation effectiveness by requiring high stimulation currents, reduces selectivity of muscle recruitment, and requires subject-specific designs to accommodate varied neuroanatomy across the patient population. Here, on a thin-film, high-channel count microelectrode array, termed SpineWrap is reported, which wraps around the dorsolateral aspect of the rat spinal cord. SpineWrap delivers focal stimulation to selectively activate muscles due to its thin substrate, high conformability, high channel count, on-device ground, and the material properties of its platinum nanorod contacts. Through computational and in vivo studies, the SpineWrap can selectively recruit muscles in the rat lower limb and identify stimulation hotspots at a submillimeter resolution, maximizing muscle recruitment selectivity. The effect of channel count and density on muscle recruitment selectivity is also investigated and show that rat spinal cord arrays require submillimeter pitches to achieve maximal selectivity. SpineWrap represents an advancement in EES technology and, when adapted to be used chronically, has the potential to improve SCI treatment by providing more refined stimulation.

1. Introduction

Understanding and controlling spinal cord stimulation is necessary for effective therapies for pain management and spinal cord injury (SCI). Epidural electrical stimulation (EES) is currently delivered with clinical paddle arrays, which were originally developed to target the dorsal columns for management of chronic pain.[1,2] More recently, EES has emerged as a promising treatment strategy and has been applied to restore motor function in animals and humans with SCI.[3–10] However, there are several technical limitations of EES applied with paddle arrays. First, paddle arrays in clinical use are made of ≈2 mm thick silicone, making these devices non-conformal to the spinal cord. This lack of conformality leads to charge spreading in the space between the paddle array and the epidural surface, reducing stimulation focality.[11,12] Second, paddle arrays have low channel counts, making it difficult to deliver stimulation at dimensions that will target small populations of sensory afferents. The electrode contacts themselves are currently made of materials with relatively high impedance and low charge injection capacity (CIC), such as platinum.[13–15] CIC is the charge per unit area that can be delivered from a given contact before the onset of irreversible electrochemical reactions at the electrode-tissue interface that can damage the contacts and surrounding

S. M. Russman, R. Montgomery-Walsh, R. Vatsyayan, H. S. U, K. Lee, S. A. Dayeh
Integrated Electronics and Biointerfaces Laboratory
Department of Electrical and Computer Engineering
University of California San Diego
La Jolla, CA 92093, USA
E-mail: sdayeh@ucsd.edu

S. M. Russman, R. Montgomery-Walsh, S. A. Dayeh
Shu Chien-Gene Lay Department of Bioengineering
University of California San Diego
La Jolla, CA 92093, USA

L. D. Diaz-Aguilar, S. Ben-Haim, J. Ciacci
Department of Neurological Surgery
University of California San Diego
La Jolla, CA 92093, USA

E. Y. Chang
Radiology Service
VA San Diego Healthcare System
La Jolla, CA 92161, USA

E. Y. Chang, Q. Tang
Department of Radiology
University of California San Diego
La Jolla, CA 92093, USA

T. L. Yaksh
Department of Anesthesiology
University of California San Diego
La Jolla, CA 92093, USA

The ORCID identification number(s) for the author(s) of this article can be found under https://doi.org/10.1002/adfm.202420488

DOI: 10.1002/adfm.202420488

tissue.[16] Therefore, scaling these electrode contacts to smaller contact areas would significantly limit their CIC and introduce additional challenges due to the voltage compliance limits of the back-end electronics used for stimulation. Finally, the resulting low contact density of paddle arrays necessitates patient-specific designs to accommodate the varied neuroanatomy across subjects,[17,18] limiting the effectiveness and the suitability of this technology for broader populations.

Previous studies have focused largely on reducing the rigidity and thickness of EES arrays to minimize foreign body response and spinal cord compression that occurs during implantation of thick and rigid arrays.[19,20] Other studies have also developed new microelectrode arrays that are fabricated on either thin polymer substrates, such as polyimide or parylene-C,[21–23] or elastomer substrates, such as polydimethylsiloxane (PDMS).[24–27] Although reducing substrate thickness and rigidity coincides with increased conformality, these arrays mostly possess channel counts on par with clinical grids and the advantages of such arrays for delivering stimulation are not clearly illustrated.

The question remains whether the efficacy of EES in selectively recruiting target muscles can be further improved with more focal stimulation. The proximity of neurons to the current source makes them more susceptible to activation at lower stimulation current intensities. Therefore, we hypothesized that bipolar stimulation using a high-density, conformal microelectrode array would more selectively target afferents in a small volume directly under the stimulating electrode contact pair and identify submillimeter hotspots for optimal stimulation. Thus, such an array would allow for more precise and more complex stimulation patterns.

Here we introduce SpineWrap, a 6.6 µm thin film, 156-channel high-density microelectrode array for targeted EES. The thinness and unique design features of the parylene-C substrate allow SpineWrap to "wrap" around the spinal cord curvature, resulting in high conformality over a large area while ensuring each electrode contact is uniformly touching the dural surface (**Figure 1**a,b). The high density and small size of SpineWrap contacts is possible because of the material properties of the platinum nanorod (PtNR) contacts (Figure 1c). We demonstrate that SpineWrap can deliver focal EES to the rat lumbar spinal cord resulting in highly selective recruitment of 6 lower limb muscles and locate stimulation hotspots for highest selectivity. We quantify the focality of SpineWrap stimulation using a computational model of the lumbar spinal cord recreated from MRI scans and show that stimulation with SpineWrap can activate tissue at depth without compromising the focality of stimulation. Finally, we evaluate the impact of channel count on muscle recruitment selectivity with post hoc channel subsampling analysis and in vivo validation studies. We show that, in rats, high-density arrays require submillimeter pitches (median = 570 µm, IQR 461–799 µm) so as not to reduce maximum achievable selectivity during bipolar stimulation across all muscles measured in this study. In its current form, SpineWrap constitutes a new, valuable research tool for probing spinal cord networks. In the future, SpineWrap has potential to improve the efficacy of EES stimulation for treatment of SCI by delivering more focal stimulation compared to clinical paddle arrays and previously developed EES microelectrode arrays.

2. Results

2.1. SpineWrap Design

The high contact density and small diameter of SpineWrap are enabled by the PtNR contact material. PtNRs have a very low impedance;[28] at 1 kHz the impedance of a 100 µm PtNR contact is 17 times lower than that of a planar platinum contact (Figure 1c). PtNRs also have high CIC; in saline, a 100 µm PtNR contact can inject up to 6 mA of current at 100 µs pulse width, which is 32 times greater than the 190 µA that can be safely injected by a planar platinum contact without causing water electrolysis (Figure 1c). In vivo, our 100 µm PtNR contacts permit the delivery of current levels up to ≈300 µA, which is enough to elicit strong muscle activation. The difference between the saline and in vivo maximum currents is a result of the different conductivities and current spreading effects between the 2 media.[29] PtNRs have been used previously for neural stimulation and recording in animals and patients in acute and chronic settings.[28,30–32] SpineWrap PtNR contacts were stable throughout the acute stimulation experiments performed in this study. The median impedance of the SpineWrap contacts was 5.12 kΩ when measured in saline. When measured on the spinal cord before stimulation, the median impedance increased to 16.3 kΩ and did not change significantly when measured again after the conclusion of the experiment, with a median impedance of 15.6 kΩ ($p = 0.29$, two-sided Mann Whitney U test, Figure S1, Supporting Information). Scanning electron microscopy (SEM) imaging of contacts before and after stimulation showed no morphological changes to the PtNRs (Figure S1, Supporting Information).

SpineWrap contact distribution can be customized and is designed here to target the dorsolateral L3-L5 spinal segments of the rat spinal cord. To design SpineWrap, we dissected the lumbar rat spinal cord to determine the average lengths of the lumbar dorsal root entry zones (DREZs, $n = 5$, Figure 1d; Table S1, Supporting Information). Based on these measurements, we determined the optimal electrode array dimensions to be 9 × 3 mm to provide adequate longitudinal and lateral coverage to the L3-L5 DREZs and account for small deviations in segmental length and electrode placement (Figure S2, Supporting Information). When determining the channel number and density of the array, we used COMSOL Multiphysics computational modeling based on an MRI reconstruction of the rat lumbar spinal cord (Figure 1d) to identify pitch ranges that resulted in focal and deep stimulation. We also considered the practical time constraint of acute studies, with each contact and current level requiring > 10 s of stimulation time. We optimized the contact layout with respect to these constraints and designed an electrode of 26 rows × 3 columns (78 contacts) on each side of the midline to arrive at a total of 156 contacts for the entire array. The horizontal (circumferential) pitch between the stimulating contacts was 500 µm and the vertical (axial) pitch was 360 µm. This array configuration allowed for complete longitudinal coverage of the L3-L5 DREZs while also extending laterally enough to cover the center points of the mediolaterally located DREZs along the circumference of the cord (Figure S2, Supporting Information), without so much

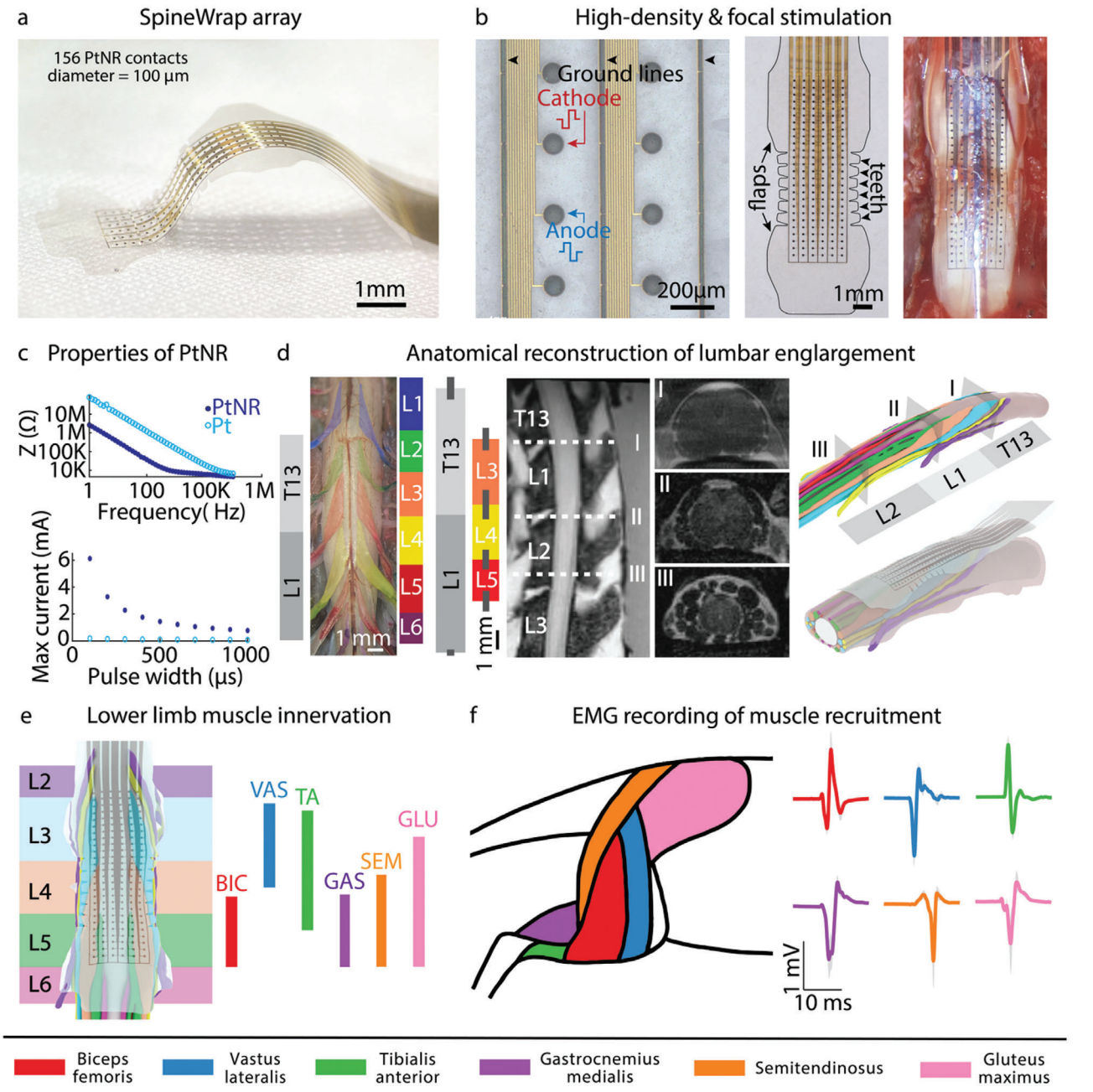

Figure 1. The SpineWrap microelectrode array for delivers focal spinal cord stimulation. a) SpineWrap design features including the 156 channel PtNR contact array with 100 µm contact diameter and 6.6 µm thick PxC substrate. b) Left: Close-up view of the microelectrode array. Stimulation was delivered in a bipolar configuration between neighboring contacts in each column. Ground lines limited current spreading. Middle: Flaps and teeth allowed for conformal placement over curved rat lumbar spinal cord. Right: Image of SpineWrap on spinal cord. c) Low impedance and high CIC of PtNRs allowed for micro-scale contact size to deliver high stimulation amplitudes. d) Dissections (n = 5) and MRI (n = 2) was used to identify the dimensions of the DREZs and guide SpineWrap design. e) SpineWrap coverage of the rat lumbar spinal cord and corresponding muscle innervation levels based on previous work.[3] f) Muscles recorded during the experiment and example trial-averaged high-amplitude EMG responses (n = 6, gray line represents ± 1 standard deviation).

lateral coverage as to compromise the conformality and uniform contact of the electrode on the entire surface of the cord. Assuming perfect placement, the L3 DREZ was covered by 66 contacts, the L4 DREZ was covered by 48 contacts and the L5 DREZ was covered by 42 contacts (Figure S2, Supporting Information). The lateral coverage of SpineWrap spanned 1250 µm from the midline, which was sufficient to provide optimal stimulation to each DREZ based on our own modeling results presented below and previous literature.[3]

To limit current spreading through highly conductive cerebrospinal fluid (CSF) that fills the space between the dura and the spinal cord surface, we delivered stimulation in a bipolar manner

along the spinal cord surface between contacts in each column of SpineWrap, with the cathode position superior to the anode (Figure 1b). In this configuration, current flowed between the adjacent electrodes, which facilitated spatially selective stimulation. Bipolar stimulation is commonly used in the clinic setting,[33] however for clinical grids the anode is set to ground. In our design, setting each anode to ground constituted a technical challenge and was impractical given the large number of contacts. Instead, the anode delivered the reverse polarity current to the cathode, thus driving current flow, and an on-device ground was placed separately on the array to sink any residual charge that is not extracted by the bipolar contacts.

In earlier studies the ground was not incorporated in the electrode design but placed separately in the paraspinal muscles (Figure S3, Supporting Information). Practical imperfection of charge balance in bipolar stimulation and the inability to fully extract injected charge led to current spreading resulting in the undesired direct activation of motoneurons, likely through the ventral nerve roots. Furthermore, while the bipolar stimulating contact can partially limit the spread of current along the axis of the spine, the lateral spread of current along the circumference of the spine is less controllable with a purely bipolar design. Direct motoneuron activation was identified by analysis of electromyography (EMG) latency (Figure S4, Supporting Information), with EMG responses appearing much sooner after stimulus in the case of direct motoneuron activation. In one of these earlier studies (Figure S3 (Supporting Information), layout 3), bipolar stimulation resulted in early latency EMG responses in some muscles, such as the vastus lateralis (median onset time 2.45 ms after stimulus, Figure S4, Supporting Information), indicating direct motoneuron activation. Since the EMG activation occurred primarily at the bottom of the electrode array at the L5 spinal level, we hypothesized that current spread to the L3 ventral nerve root, which was in a lateral position at the L5 spinal level and innervates the vastus lateralis. We confirmed that current spread was significant in the earlier designs by shifting the position of the ground needle in tissue (Figure S5, Supporting Information). Depending on the location of the ground needle, we observed a change in the contacts eliciting muscle activation.

We modeled the spread of current using COMSOL simulations for a reconstructed model of the rat spinal cord. To determine the L3-L5 nerve root organization and overlap and to preserve their in situ trajectory, we imaged the intrathecal lumbar and sacral nerve root organization using MRI (Figure 1d; Figure S6, Supporting Information). We then reconstructed a 3D anatomical model to serve as the basis for our finite element modeling to calculate field-distributions and imported the model into COMSOL. In COMSOL, we gave each tissue an electric conductivity based on previously reported values[34,35] (Table S2, Supporting Information). We modeled stimulation with and without charge mismatch to illustrate the advantage of electrode arrays with and without an on-device ground (Figure S7, Supporting Information). We found that charge mismatch significantly reduced stimulation focality without on-device ground.

These results led us to redesign the electrodes to incorporate the ground adjacent to the stimulating electrode contacts to create an on-device ground. An on-device ground was critical for the focal stimulation and selective activation of DREZs. This was included in the form of ground lines between columns of contacts (Figure 1b, middle). In subsequent experiments, the electrode with on-device ground lines did not show any current spreading, with significantly higher latency EMG responses recorded even at the highest current levels (median onset time 4.85 ms after stimulus, $p < 0.05$, two-sided Mann Whitney U test; Figure S4, Supporting Information). This indicates indirect motoneuron activation through sensory afferents. Thus, with its on-device ground, SpineWrap provides focal stimulation without current spread.

In designing the on-device ground, we explored both a concentric ground ring around each contact and in-plane groundlines in between rows of contacts. The concentric ground design was previously proposed as a method to deliver highly focal cortical stimulation.[36] In our experiments, concentric ground did not result in EMG response amplitudes that were as high as for ground lines (Figure S8, Supporting Information). We concluded that the distance between the stimulating contact and surrounding ground was too small for even high stimulation currents to reach sufficient depths to recruit enough afferent fibers to produce large EMG responses. This resulted in a tradeoff between cathode-to-ground pitch and contact density. Therefore, we opted for vertical ground lines on SpineWrap to not compromise the high density we aimed to achieve.

For focal stimulation, it was critical that SpineWrap wraps conformally onto the spinal cord surface to ensure uniform contact of all electrode contacts and ground lines on the array and therefore generate consistent stimulation across all contacts. Uniform conformality across all contacts was a challenge since the array needed to capture enough longitudinal and lateral coverage of the DREZs while also allowing for longitudinal bending along the axial curvature present in rats at the L3-L5 spinal segments. We tested many iterations of the electrode array design to achieve a conformal device (Figure S3, Supporting Information). We ultimately opted for a device design that had 2 flaps in the upper and lower regions (Figure 1b, middle). These flaps allowed the electrode to latch onto the L3-L5 spinal levels while omitting the T13-L1 vertebral bone junction, which was left intact to not damage to the nerve roots exiting at this location. Between the flaps, teeth were etched into the lateral edge of the array to relieve buckling of the flat parylene C film. Ultimately, this design allowed for consistently conformal placement of SpineWrap across animals (Figure 1b, right). During stimulation, we additionally placed gel foam onto the electrode surface and the surrounding tissues. This has kept the epidural surface moist and the electrode in place. We compared the placement of the electrode before and after the stimulation to confirm the electrode placement did not shift during stimulation (Figure S9, Supporting Information).

2.2. Stimulation Focality of SpineWrap

We used SpineWrap to recruit lower limb muscles in anesthetized intact rats. Stimulation was delivered via the Intan RHS Stim/Recording System and a custom-designed PCB with a BGA clamshell socket (Figure S10, Supporting Information). The SpineWrap connector region was aligned to the BGA under an optical microscope. Once SpineWrap was well aligned in the socket, the clamshell socket lid was closed, making contact between the SpineWrap connector area and the BGA. The use of

the clamshell socket eliminated the necessity of using epoxy to bond the connector region to the PCB, reducing risk of shorts due to epoxy spreading.

We stimulated at 0.5 Hz in a semi-random order and recorded muscle activity with bipolar EMG needles in 6 muscle groups innervated by the L3-L5 spinal segments:[3] biceps femoris (BIC), vastus lateralis (VAS), tibialis anterior (TIB), gastrocnemius medialis (GAS), semitendinosus (SEM) and gluteus maximus (GLU) (Figure 1e,f). We computed the peak-to-peak (PTP) EMG amplitudes of the recorded response waveforms. PTP amplitudes were normalized (PTP_{norm}) by dividing them by the maximum peak-to-peak amplitude (PTP_{max}) across current levels (see Methods) to perform inter-muscular and inter-animal analysis. We performed stimulation on both left and right sides of the spinal cord in 2 rats (referred to as datasets Rat 1r/l and Rat 2r/l) and on the right side only in 2 rats (referred to as datasets Rat 3r and Rat 4r). Since in this study we investigated general trends in muscle segmental activation and selectivity without emphasis on precise mediolateral contact position, we grouped the left and the right datasets from different animals in our analysis to arrive at total of 6 datasets for this study.

We varied stimulation currents between 15–300 µA and measured the EMG responses. At low current levels, only a few pairs of bipolar contacts showed muscle activity at the corresponding spinal cord segmental level (**Figure 2**a–c,e,f). Increasing the stimulation current increased the number of bipolar pairs of contacts generating significant muscle response. As the current amplitude was increased, nearest neighboring bipolar contact pairs to those initially selective to specific muscles at lower amplitudes began to also elicit muscle responses, with highest current levels generating responses across many bipolar contact pairs and multiple segmental levels. We defined the current amplitude thresholds necessary to generate a significant muscle response as those resulting in an EMG response with $\geq$ 0.1 PTP_{max} and identified the median current threshold to be 35–50 µA across muscles (Figure 2d).

We hypothesized that at low current levels there are few contacts eliciting muscle activation because the stimulation is very focal and only targets the sensory afferents directly under the bipolar contact pair. Increasing the stimulation current amplitude activates afferents further from the bipolar contact pair, thus many multiple pairs can activate the same afferents, resulting in widespread muscle activation. We used finite element modeling in COMSOL Multiphysics to illustrate this effect by increasing stimulation from a pair of contacts and the plotting resulting potential (Figure 2g). To do this, we imported a 3D construction of the MRI imaged rat lumbar spinal cord into Blender, and individual spinal elements were then converted into.stl files and used in COMSOL Multiphysics (See Methods, Computational Modeling). Even at 250 µA current levels, there was no appreciable potential within the spinal cord white matter that would cause activation, with significant potential gradients only in the CSF.

2.3. Muscle Recruitment Selectivity

To assess the impact of SpineWrap's focal stimulation on selective muscle recruitment, we computed the selectivity index (SI) for each muscle and each contact using previously published equations for selectivity,[37] where SI is the difference between PTP_{norm} for each current level, contact, and muscle and the mean PTP_{norm} of the remaining muscles (see Methods). Across datasets, we found that the SI distribution generally agreed with spinal innervation (**Figure 3**a; Figure S11, Supporting Information). The SI distribution per muscle skewed toward zero for most muscles and most datasets, with few channels per electrode eliciting high selectivity (Figure 3b; Figure S12, Supporting Information). Additionally, in some locations on the array, SI values varied significantly between neighboring contacts, indicating that stimulation from neighboring contacts activated distinct sets of muscles (Figure 3c).

We extracted the maximum SI (SI_{max}) per channel for each muscle and each dataset and overlaid the channel locations of SI_{max} (Figure 3d; Figure S12, Supporting Information). The locations of SI_{max} were closely distributed and corresponded to the expected muscle innervation. Exceptions were Rat 2r, where the SEM and GLU SI_{max} were positioned in the upper part of the array and Rat 4r, where the GAS SI_{max} was positioned in the upper part of the array (Figure S13, Supporting Information). To determine the average SI_{max} achievable with the SpineWrap array, we compared SI_{max} values across the datasets. We found that the average SI_{max} was $\geq$ 0.5 for all muscles (Figure 3e), indicating that the SpineWrap array could achieve moderate to high selectivity across all 6 muscle groups recorded in this study.

A motivator for this study was the hypothesis that the high-channel count of SpineWrap would result in more options for channel selection and point to hotspots of maximal selectivity, thus optimizing the stimulation locations compared to conventional, low-channel count paddle arrays. The SI distributions in Figure 3b indicate that SpineWrap can identify hotspots with very high selectivity. To further evaluate this hypothesis, we investigated how selective the SI_{max} channels were compared to the remaining SIs. Across datasets and for each muscle, we identified contacts with comparable SI value to SI_{max} by calculating the number of contacts per dataset that had an SI $\geq$ 90% of SI_{max}. We found that the median number of bipolar contact pairs with a comparable SI value across datasets was between 1–3 per muscle (Figure 3f). Thus, we conclude that SpineWrap's high-density coverage can pinpoint to a few hotspot locations for highest muscle recruitment selectivity.

2.4. Effect of Array Channel Count and Resolution on Recruitment Selectivity

Improving stimulation focality by increasing channel count and resolution has been a topic of interest in the neuromodulation community. However, to the best of our knowledge, this effect has never been quantified for spinal cord stimulation. Though our SI values indicate selective muscle recruitment, SI values are difficult to directly compare to previous studies using lower density arrays due to differences in experimental design and recorded muscle groups. We explored an alternative method for quantifying the impact of both channel count and resolution on stimulation selectivity.

We subsampled the SpineWrap array using Poisson Disk sampling and computed subsamples of 4–36 bipolar contact pairs (n = 1000). The resultant range of pitches between the bipolar

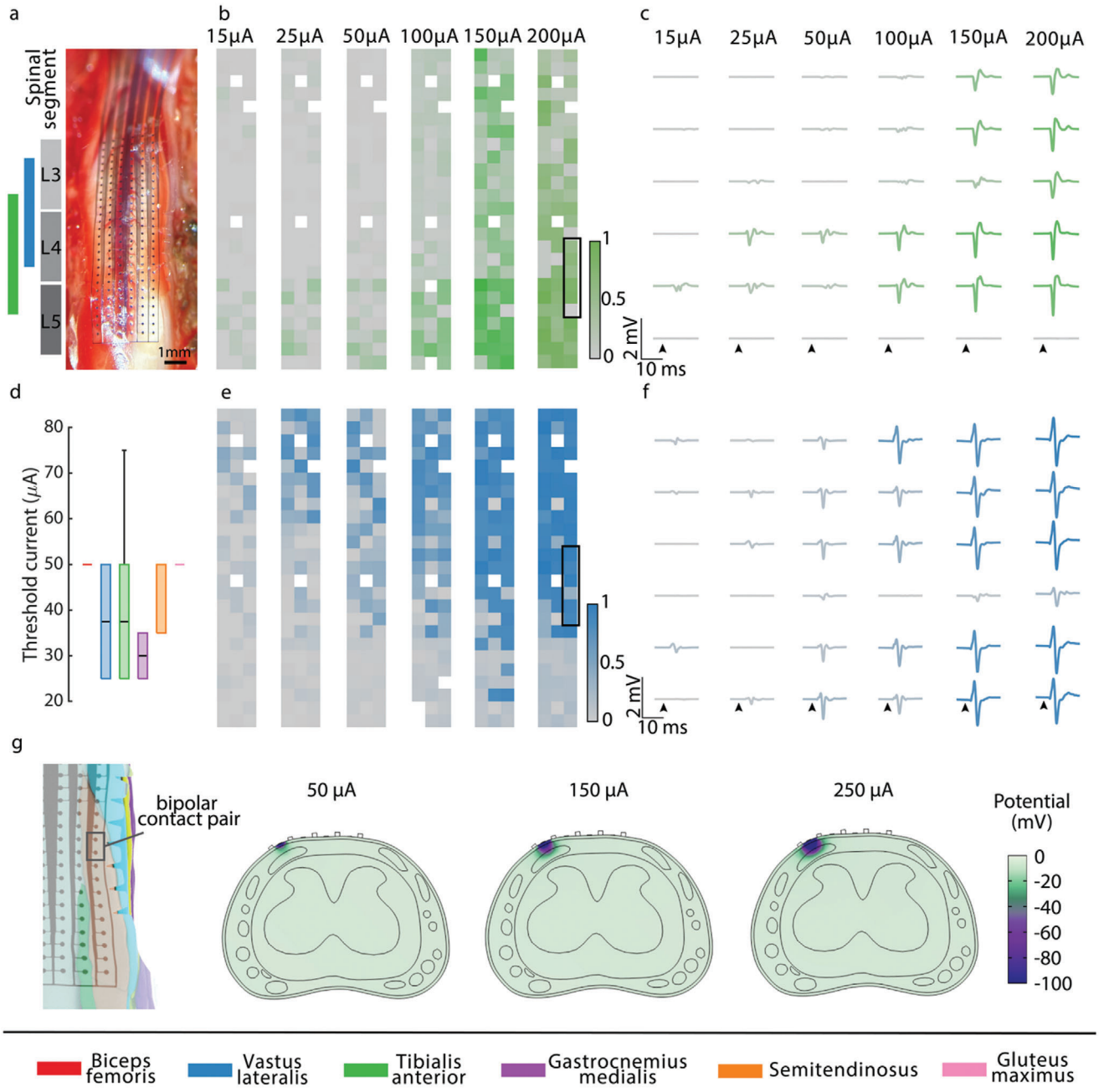

Figure 2. SpineWrap delivers focal spinal cord stimulation. a) Placement of SpineWrap on spinal cord for Rat 3r and approximate locations of innervations for muscles tibialis anterior (green) and vastus lateralis (blue). b) Increasing current amplitude results in widespread activation of TIB. c) Close-up view of the black box in (b) with plotted trial-averaged EMG waveforms. Black arrows indicate stimulation time. d) The stimulation current threshold necessary to produce a significant EMG response (≥0.1 PTP_{max}, $n = 6$) for each muscle. Each boxplot shows the distribution of the current threshold for a given dataset and muscle. The horizontal center lines and boxes indicate the median and the 25th/75th percentile and the vertical solid lines represent the full range of the distribution. e) Increasing current amplitude results in widespread activation of VAS. f) Close-up view of the black box in (e) with plotted trial-averaged EMG waveforms. Black arrows indicate stimulation time. g) Modeling results from COMSOL quantifying the focality of stimulation delivered by a pair of electrodes on the L4 DREZ at increasing current levels.

contact pairs (termed inter-cathode pitch) was 624.5–1873 μm (see Methods). We then evaluated the SI_{max} of these subsampled datasets (**Figure** 4a). Reducing the number of bipolar contact pairs available for stimulation reduces the median SI_{max} of the subsamples (Figure 4b; Figure S14, Supporting Information). We fit a 4th degree polynomial to the median SI for each pitch and each muscle and extrapolated the minimum inter-cathode pitch necessary to achieve ≥ 90% SI_{max} of the original array. The minimum pitch to not reduce SI_{max} of the subsample was 570 μm, which is the median minimum pitch required

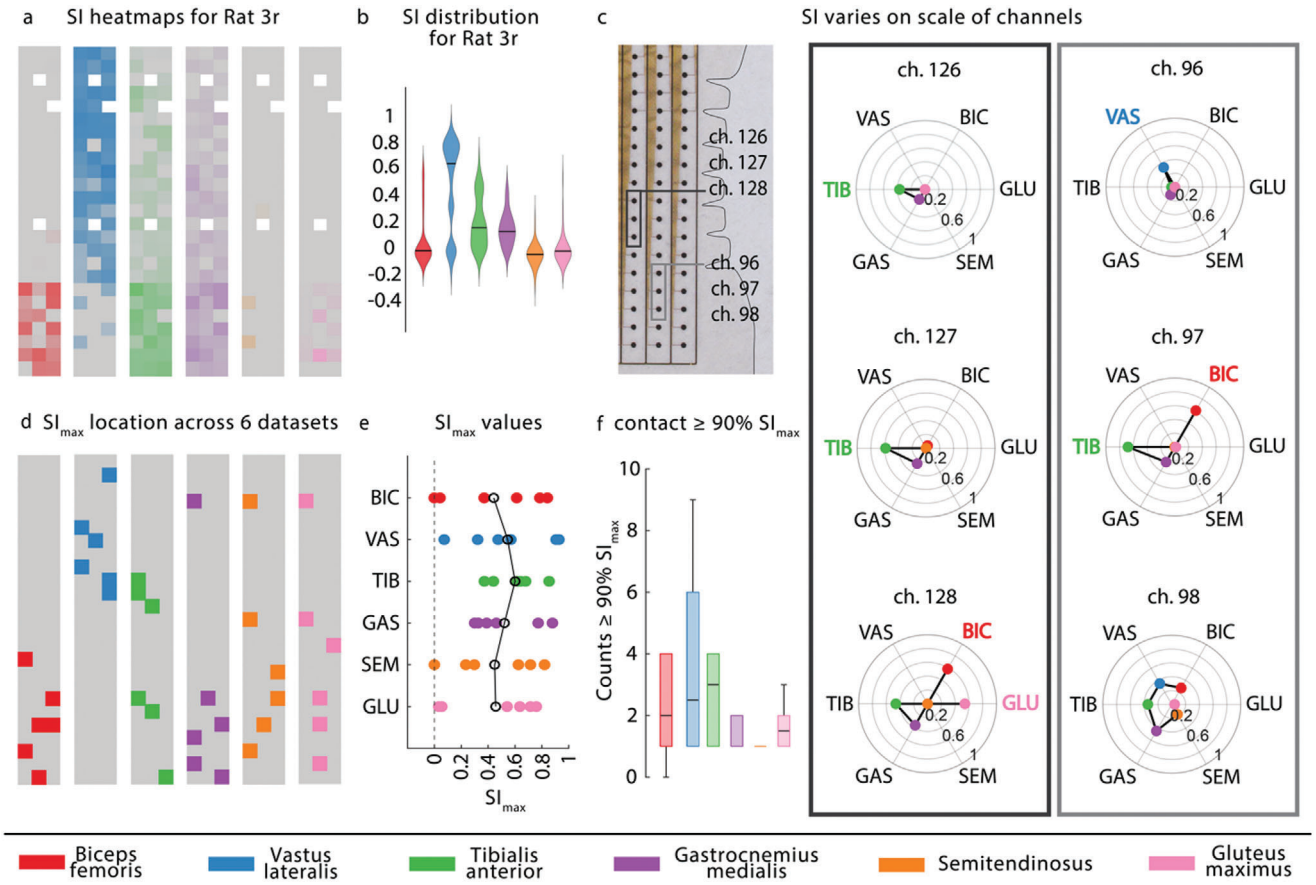

Figure 3. SpineWrap produces selective lower limb muscle activation. a) Example SI distribution across electrode arrays for all muscles for Rat 3r. b) The distribution of selectivity indices for Rat 3r. c) Selectivity can vary on the scale of individual channels, with neighboring channels recruiting different muscles more selectively. For example, the dominant muscle shifts from TIB at channels 126 and 127 to BIC and GLU at channel 128. Similarly, the dominant muscle shifts from VAS for channel 96 to TIB and BIC for channel 97. At channel 98, no muscle is highly selective. d) Comparison of cathode locations of bipolar contact pairs that produced SI_{max} for each muscle across all datasets. e) SI_{max} values for each muscle across all datasets ($n = 6$). The open black circles are the mean SI_{max} for each muscle, and the black line connects the mean SI_{max} from the different muscles. f) The number of bipolar contact pairs that have SI values close to SI_{max}. Each boxplot shows the distribution of the number of pairs with SI values ≥90% of SI_{max} for each dataset ($n = 6$ datasets) and muscle. The horizontal center lines and boxes indicate the median and the 25th/75th percentile and the vertical solid lines represent the full range of the distribution.

for SEM (Figure 4c, IQR 461–799 µm). Unlike previously developed low-density rat EES arrays,[22,38] SpineWrap possesses a pitch smaller than this minimum pitch. Therefore, we conclude that the electrode design does not contribute to reduction of SI.

2.5. Validation of High-Channel Count Array Benefits with In Vivo Experiments

We validated the subsampling results with an in vivo study. We fabricated a similar array to the SpineWrap array, but we increased the horizontal and vertical pitch of the contacts from 500 and 360 µm to 1000 and 800 µm, respectively. The resulting channel count of this array was reduced from 156 contacts to 40 contacts and the resulting density dropped from 5.6 to 1.42 contacts mm^{-2}. The mean pitch (see Methods) increased from 424.3 to 837.9 µm, falling well outside of the 570 µm minimum pitch identified in the subsampling analysis. We increased the contact diameter from 100 to 500 µm to match the contact area more closely in previously developed low-density rat EES arrays.[22,38] The array coverage, shape, thickness and ground lines design were the same as those of SpineWrap to limit variability in results due to conformality, placement, and grounding (Figure S15, Supporting Information).

We performed additional stimulation with the low-density array in Rats 2r/l and 4r. Current levels up to 1 mA were used while staying within the charge injection limit of the larger diameter. For analysis, we aligned the electrodes based on blood vessel patterns on the spinal cord surface (**Figure 5a**). We compared the SI value range of the 2 arrays and found that the distribution was narrower for the low-density array across all muscles (Figure 5b), highlighting that SpineWrap can identify stimulation hotspots to maximize SI. SI_{max} was larger for the high-density array compared to the low-density array, as indicated by the ratio between the low-density and high-density values (Figure 5c, see Methods). Notably, this empirical data shows a larger impact of channel count on selectivity than the subsampling analysis

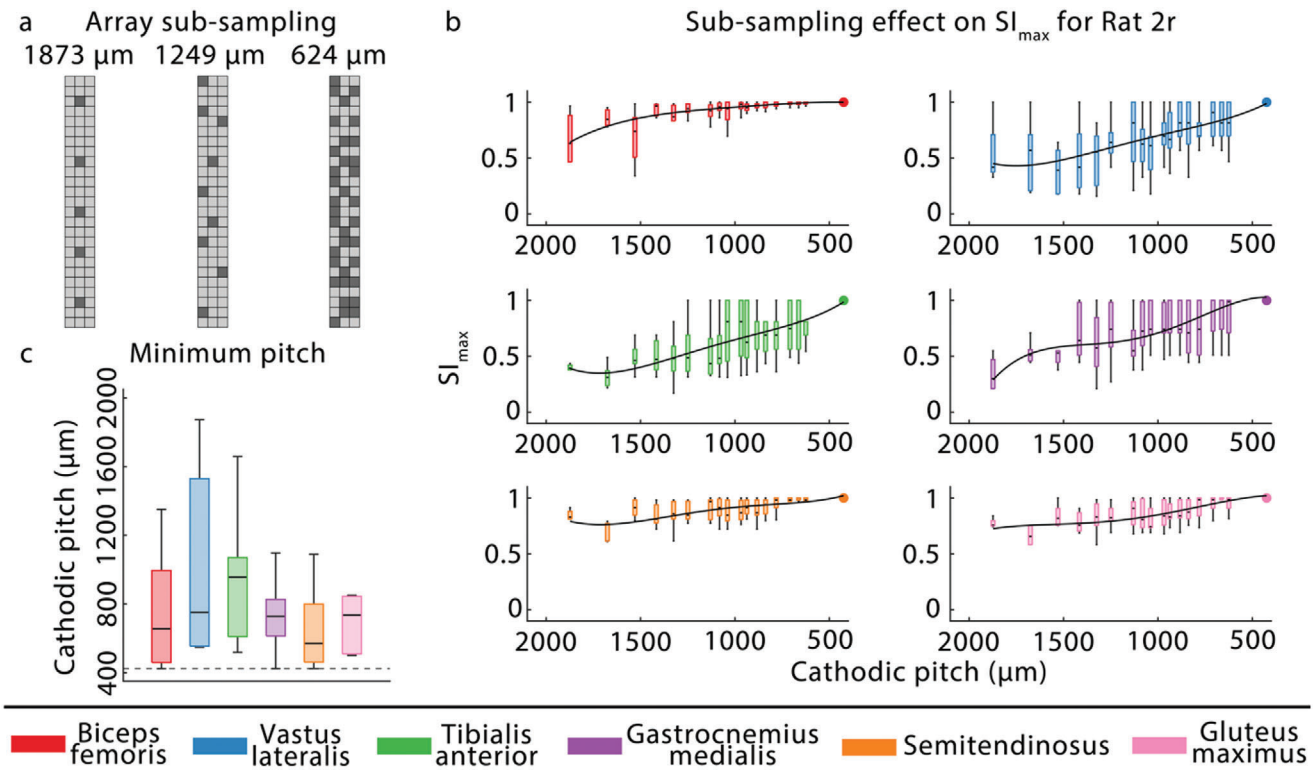

Figure 4. Muscle recruitment is more selective with high-spatial resolution and high-channel count spinal cord coverage. a) Example subsamples of the array at various cathodic pitches (n = 1000 subsamples obtained using Poisson Disk sampling). b) Median maximal recruitment selectivity, measured as the ratio of the subsample SI_{max} to the SI_{max} of the full array, increased with smaller decreasing inter-cathode pitch. The horizontal center lines and boxes indicate the median and the 25th/75th percentile and the vertical solid lines represent the full range of the distribution. Note that at the smallest pitch there is only one datapoint, which is the SI_{max} of the full array. Sub-sampling results are from Rat 2r. c) The minimum inter-cathode pitch required to not reduce the median SI_{max} of subsamples across all muscles was 570 µm (minimum pitch for SEM). Dashed line represents the pitch of SpineWrap.

predicted, albeit for a particular choice of design parameters. At an inter-cathode pitch of 838 µm, the subsampling analysis predicted SI_{max} ratios ≥ 0.7 for all muscles whereas the in vivo data produced ratios less than that for most muscles. This may in part stem from non-linear effects of inter-cathode pitches on selectivity that are not captured in the post hoc subsampling analysis and in part from the larger contact diameter, resulting in stimulation delivered over a larger surface area. Moreover, the subsampling analysis did not account for changes in pitch between the cathode and anode (termed cathode-anode pitch) of each bipolar contact pair as the inter-cathode pitch increased; instead, the cathode-anode pitch remained 360 µm, whereas the cathode-anode pitch of the low-density array increased to 1000 µm. In conclusion, the in vivo results confirm that higher-channel count and higher-density electrode arrays improve muscle recruitment and selectivity and reduce the necessary current amplitudes for stimulation.

2.6. Modeling the Effect of Contact Diameter and Spacing on Potential Gradients

Each design parameter for the electrode, including the contact-to-contact pitch (both circumferentially and axially) and the spacing between contact and ground lines, has a significant impact on the measured focality of stimulation. Practically, it is impossible to cycle through all possible design choices in vivo. Therefore, to predict the impact of the electrode design parameters on focality, we compared the spread of potentials and the width and the depth of afferent axon recruitment to various contact arrangements using computational modeling in COMSOL. First, we computed the potential profiles consistent with the stimulation paradigms that we employed in vivo (Figure 5d). We observed that with larger diameter contacts, the potential spreads more laterally, which effectively reduces the selectivity of stimulation, consistent with the experimentally observed results. Larger contacts have the capability of injecting significantly higher currents, but the selectivity of stimulation is greatly reduced at the same charge density (318.3 µC cm^{-2}). This highlights the benefit of using smaller diameter low-impedance materials for focal stimulation.

We evaluated the relationship between stimulation depth versus width. We used a previously published approximation of axon activation to unipolar stimulation to identify a threshold potential for afferent activation. This method relies only on the extracellular potentials of the node under the stimulating cathode and the neighboring nodes.[39] The threshold potential was found to be 28 mV for a 10 µm diameter axon with internodal distance of 900 µm (Figure S16 (Supporting Information), see Methods). This axon diameter and internodal distance correspond to the

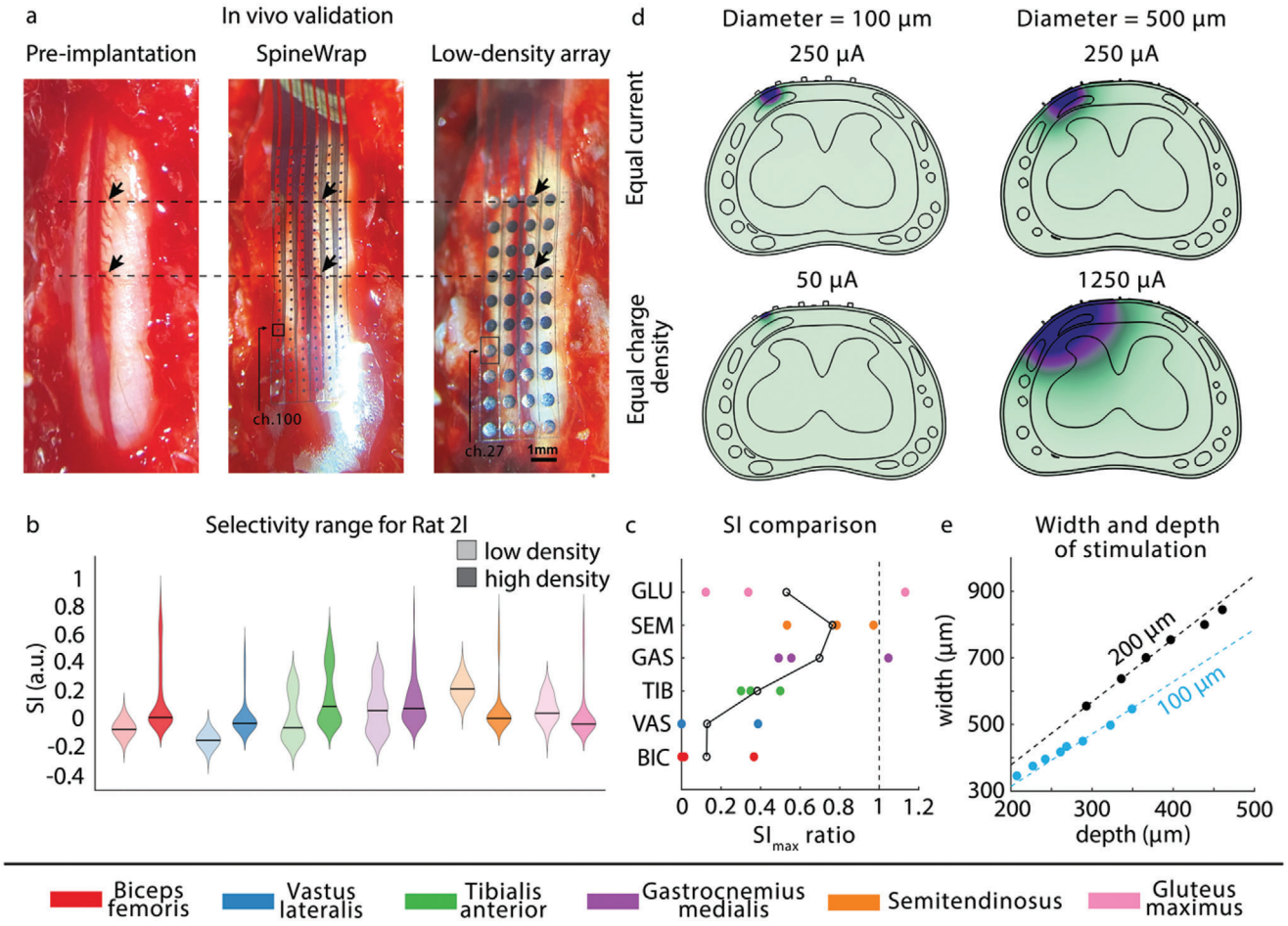

Figure 5. In vivo validation of high-channel count effect on muscle recruitment selectivity. a) Placement of SpineWrap and the low-channel count array for Rat 2. Arrays were aligned in post-processing based on vasculature on the spinal cord surface highlighted with black arrows. b) SI range for both arrays for Rat 2r. c) Comparison of SI_{max} ratio between SpineWrap and the low-channel count array. Low-channel count array SI values are divided by SpineWrap SI values. The open black circles are the mean SI_{max} ratio for each muscle, and the black line connects the mean values from the different muscles. d) Computational modeling of equal current and equal charge density delivered from 100 and 500 µm diameter bipolar contact pairs. e) Stimulation depth versus stimulation width for 100 and 200 µm diameter bipolar contact pairs.

size of the group I fibers in the rat spinal cord, which travel through the dorsal roots and DREZs.[34] This threshold potential was used to evaluate stimulation depth versus width of 100 and 200 µm bipolar contact pair arrangements (Table S3, Supporting Information). Although changing the dimensions of the contacts and the contact spacing will the affect potential gradient, which in turn affects the threshold potential, we chose 28 mV as the threshold across all bipolar contact pairs and currents tested as a reference for measuring stimulation depth and width consistently between different contact sizes without introducing additional dependent variables. Our results show that smaller diameter contacts with on-device ground lines stimulate deeper with lower lateral spread than larger diameter contacts (Figure 5e).

3. Discussion

SpineWrap is, to the best of our knowledge, the highest channel-count and highest density spinal cord microelectrode array for EES to date. SpineWrap was able to deliver focal stimulation to selectively activate muscles due to its unique design features, including its thin substrate, conformability, channel count, on-device ground, and the material properties of its PtNR contacts. We quantified the focality of the delivered stimulation through computational modeling. In vivo recordings in rat spinal cord stimulations further supported these results. We showed that SpineWrap selectively recruited all 6 lower limb muscles recorded in this study, with median SIs $\geq$ 0.5. We showed that SpineWrap can elucidate hotspots for optimal stimulation at sub-millimeter resolution, on the scale of individual 100 µm contacts. Finally, we performed post hoc analysis and additional in vivo studies to determine that high-channel count improves selectivity.

In our subsampling analysis, the minimum inter-cathode pitch before significant loss in selectivity (SI $\leq$ 90% SI_{max}) was observed was 570 µm. Given that the L3-L5 DREZ lengths range from 3.28 $\pm$ 0.67 mm for L3 to 2.40 $\pm$ 0.40 mm for L5, this indicates that at minimum 5–7 contacts must cover each DREZ longitudinally to achieve the same SI results. One limitation in

this analysis is that the inter-cathode pitch did not reflect the cathode-anode pitch as these were determined physically by the electrode design. As a result, the delivered stimulation was more focal than would be the case with a lower channel count array and larger cathode-anode pitch than the subsampling analysis predicted. We accounted for this limitation in the in vivo validation studies. We confirmed selectivity is reduced in lower channel count arrays with in vivo studies, where we compared SpineWrap stimulation capabilities to a lower density array with only ≈3 contacts in the longitudinal direction per DREZ. We showed that the high-density SpineWrap indeed outperformed the low-density array in stimulation focality and selective muscle recruitment.

The results we report here on contact density and selectivity are proof-of-concept and should not be generalized. In particular, the low-density array we used to compare to the high-density SpineWrap was thin film, thus it likely delivered stimulation in a different manner than thicker paddle arrays. Further studies investigating the impact of contact density on selectivity will be performed to fully explore this relationship. Additionally, since the low- and high-density arrays could not be placed simultaneously on the spinal cord, the stimulation delivered from the low-density and high-density arrays could not be randomized. Therefore, there could be unaccounted for effects of time on the results we report here. However, across studies, we did not observe an effect of time on EMG amplitude, therefore we expect this effect to be minimal. Additionally, for the width versus depth analysis, we used a threshold of 28 mV. The threshold for activation is dependent on the spatial distribution of the potential field, therefore this value is not the de facto threshold and is used only to standardize the potential gradient analysis.

To translate SpineWrap for SCS in the chronic setting, methods of integration of SpineWrap with implantable pulse generators (IPGs) need to be developed. In our study, we first focused on demonstrating unequivocally the benefits of using microelectrode arrays in focal stimulation. Armed with these results, we will next focus on the long-term application of these arrays for long-term implants. In this study, we used a complex benchtop stimulation setup that relied on the Intan RHS Stim/Recording System, which is limited to 128 stimulation channels, and a large PCB to interface with the electrode (Figure S10, Supporting Information). Since our electrode contained more than 128 channels, we only stimulated one half of the array at a time. In its current format, this setup could not be used in awake animal and human subjects. Commercially available implantable IPGs that enable continuous stimulation in awake animal and human subjects can only stimulate up to 16 channels. Consequently, to fully utilize SpineWrap's high-channel count in a clinical context, further development of more advanced IPGs is essential, and SpineWrap is currently an EES research tool rather than a therapeutic one.

Our mechanistic study of stimulation focality and contact density effects on muscle recruitment selectivity was performed in anesthetized animals. Future work will use SpineWrap in awake animals. Literature has shown that the co-activation of muscles can differ between anesthetized and awake animals and this co-activation can also be affected by SCI.[40,41] Thus, some results in our study, such as the specific SI values, may not directly translate to awake animals and human subjects with SCI. Although in this study we did not validate the functionality of SpineWrap chronically, previous studies have successfully deployed thin film parylene-C electrode arrays in the spinal cord with minimal spinal compression and foreign body response, and the arrays remained functional after many weeks.[22,23] Therefore, we believe SpineWrap will be stable long-term and lead to minimal damage to the spinal cord.

Another future direction is to tailor SpineWrap's form factor to larger animal models and humans. Modifications to shape and contact arrangement will be necessary to ensure enough coverage while maintaining high conformality and muscle selectivity. However, PtNR arrays with hundreds and thousands of contacts have been previously used for brain and spinal cord recordings.[22,23] Therefore, creating a larger coverage array with similar density for human use should be possible. The implications of high-channel count microelectrodes for EES in humans need to be additionally explored in future studies since the contact density in humans can be even greater than in rats given that the human spinal cord is much larger in cross-sectional area and the DREZs are larger as well.[42] The axon diameters of human afferents are also larger,[43] and the human dura is thicker,[44,45] which may affect the minimum contact pitch required to maximize muscle recruitment selectivity in humans.

In this study, we did not investigate the effect of stimulating multiple channels in spatial or temporal configurations. Prior work has shown that spatial and temporal summation of neural recruitment due to stimulation is nonlinear,[46–51] thus there could be beneficial, compounding effects of highly focal EES. Spatiotemporal stimulation with paddle arrays mimicking natural spinal cord activation patterns during locomotion has resulted in functional restoration of movement in animals and patients with SCI.[3,48] The use of a high-channel count microelectrode array such as SpineWrap could provide a more sophisticated recording of intact spatiotemporal spinal cord activity. Higher density grids could also reproduce these sophisticated patterns with fine-tuned stimulation to produce more refined movements. In this study, the time to perform stimulation and data analysis was limited due to the acute nature of the experimental setup. This prevented the exploration of multichannel stimulation effects. Additionally, the benefits of spatiotemporal stimulation paradigms are most pronounced in awake subjects who can volitionally produce movements,[40,51] therefore its benefits would not have been clear in our studies in anesthetized rats. Future studies will investigate the potential compounding effects of multichannel, spatiotemporal stimulation in awake rats with SCI. However, even with single channel stimulation, the improvement in stimulation focality and muscle recruitment selectivity with high-channel count and high-density microelectrode arrays was still apparent in our results.

In summary, our findings indicate that SpineWrap greatly improves stimulation focality and muscle recruitment selectivity compared to the conventional clinical paddle arrays currently employed to deliver EES for treatment of SCI. Consequently, the adoption of SpineWrap in EES treatment has the potential to push the boundaries of current EES technology and offer more efficient therapies.

4. Experimental Section

Vertebrate Animal Subjects: Adult (> 5 months old, weight range 500–650 g) male Sprague-Dawley rats (Charles River Laboratories) were used as vertebrate animal subjects in this study. All animal experiments were approved by the UC San Diego Institution Animal Care & Use Committee (protocol S16020).

Fabrication of SpineWrap: SpineWraps were fabricated in small batches on a 7″ × 7″ × 0.06″ photomask-grade soda lime glass plate (Nanofilm), which were cleaned via O_2 plasma at 200 W for 5 min. The plate was coated with 3.7-µm-thick-parylene C using a parylene deposition system (Specialty Coating Systems 2010 Labcoater). Next, 2 layers of gold traces (10 nm Cr, 150 nm Au) were deposited onto the plate using standard lithography techniques and AZ5214E-IR photoresist (MicroChemicals). This double layer of leads was found to improve device yield by reducing chance of disconnects due to particles during the photolithography process.

PtNR contact formation on parylene-C was done using a technique previously developed and described in our previous publications.[30,31] Briefly, the metal traces and PtAg alloyed contacts were encapsulated in a second 3.1 µm parylene layer. After deposition of a Ti hard mask, the PtAg contacts and connector pads were exposed by dry etching the Ti layer in the exposed regions with SF_6/Ar gas, followed by oxygen dry etching of the parylene C. The entirety of the Ti layer etching as well as the sample release from the substrate was achieved with dip in 6:1 buffered oxide etchant (BOE) and the PtAg was dealloyed in 60 °C heated nitric acid for 2 min, thereby forming the PtNRs with Pt/Ag composition of ≈95%/5%.

Evaluation of Electrochemical Properties of SpineWrap: Impedance magnitude and phase at 1 kHz was measured in saline and in tissue before and after stimulation using the RHS Stim/Recording System (Intan Technologies). The EIS spectrum and CIC of the PtNR contacts was measured in 3-point configuration with a Pt counter and Ag/AgCl reference using the Reference 620 potentiostat (Gamry Instruments).

Scanning Electron Microscopy Imaging: The Apreo HiVac SEM was used to image the PtNRs on the electrode surface before and after stimulation in vivo. Samples were sputtered coated with iridium before imaging. Images were taken at ×10000 magnification, a working distance of 10.5 mm, and an accelerating voltage of 3 kV.

Spinal Cord Dissections: Male Sprague-Dawley rat spinal cords ($n = 5$), including the T11-L6 vertebral segments, were extracted after euthanasia and placed in 4% phosphate buffered paraformaldehyde (PFA). After one week of fixation, spinal cords were dissected to identify spinal segments and DREZ locations. The vertebral bone was removed to reveal the entire dorsal aspect of the spinal cord and access nerve roots at their exit point from the vertebral column. The dura mater was cut along the rostrocaudal axis to access the nerve roots. Nerve roots were identified by their exit point from the vertebral canal and traced rostrally to the entrance into their spinal segment. DREZs and vertebral segments were labeled by color, measured along their rostrocaudal length, and optically imaged.

MRI Reconstruction: A male Sprague-Dawley rat weighing 650 g was perfused transcardially with phosphate buffered saline (PBS) followed by 4% phosphate buffered paraformaldehyde (PFA) to achieve tissue fixation. The spinal cord, from the T12 to S1 vertebral segment, was extracted and placed in 4% PFA for one week and subsequently transferred to PBS. The MRI scan was performed using a Bruker 3 Tesla scanner with a 40 mm volume coil and an axial resolution of at least 0.08×0.08×0.3 mm. Nerve roots were identified in 3D Slicer at their exit point from the vertebral canal and traced rostrally to their entry point into the spinal cord. 3D reconstructions of intrathecal nerve root trajectories were built using MRI segmentation tools in 3D Slicer.

Computational Modeling: The 3-D reconstruction of the rat lumbar spinal cord was imported into Blender and individual spinal elements were converted into.stl files to be imported into COMSOL Multiphysics. To manage the complexity of simulations, only the T13-L1 section of the spinal cord was simulated. The electrode contact material was assigned to be platinum, and the electrode-tissue interface was not modeled. For consistency, the stimulating electrode injecting the cathodic-first current was always in the same longitudinal and lateral location on the spine. The stimulating contacts and the ground lines were assumed to be in direct contact with the dura mater. Time domain current analyses were performed using the Electric Currents (ec) physics module. The simulation results were exported into MATLAB for post-processing and visualization.

Determining Activation Threshold for Potential Gradient Analysis: The width and depth of the stimulation area was calculated by thresholding the resulting potential gradients by 28 mV. Axon activation was estimated using the second spatial difference $\Delta^2 V_e(n)$ approximation at node n from Peterson et al.[39] as follows:

$$\Delta^2 V_e\ (n) = V_e\,(n-1) - 2V_e\,(n) + V_e\,(n+1) \tag{1}$$

where $V_e(n-1)$, $V_e(n)$, and $V_e(n+1)$ are the extracellular potentials at 3 neighboring nodes $n-1$, n, and $n+1$.

An exponential decay curve was fitted to the 10 µm diameter data from Peterson et al. to identify the threshold relationship between the extracellular potential and the second spatial difference (Figure S15b, Supporting Information). Next, the potential gradients from 100 µA unipolar, cathodic stimulation were computed at 3 node locations: in the x,y plane of the electrode contact (the center node was located below the electrode), and 900 µm in either z-direction, where the closest neighboring nodes were located. The internode distance for a group I sensory rat afferent has previously been estimated to be 900 µm.[34] In this analysis, we assumed the center node was directly below the electrode contact, which should have limited effect on the activation threshold since previous analysis showed that significant errors in threshold occurred only at large alignment offsets. The resulting distribution of extracellular potentials and corresponding second spatial differences were plotted and 2nd degree polynomial was fit to the data. The intersection point between the threshold curve and the 2nd degree polynomial was regarded as the threshold potential (Figure S15f, Supporting Information).

Surgical Procedures: Rats were sedated with 4% isoflurane and fixed in a stereotaxic frame (Kopf Instruments). Once stable, anesthesia was reduced to 1.5%–2.5% during the surgery. A laminectomy was performed on the T12-L2 vertebral segments, exposing the dorsolateral surface of the spinal cord without breaching the dura. The SpineWrap array was implanted over the T13-L1 vertebral segments, corresponding to the L3-L5 spinal segments. Gel foam was used to cover the microelectrode array and the surrounding tissues to secure it in place and maintain moisture on the cord. Bipolar needle EMGs were placed in both left and right muscle groups of the lower limbs.

Once the surgery was completed, rats were transitioned from isoflurane to ketamine/xylazine (90 and 10 mg kg^{-1}, respectively; MWI) and redosed 20–30 min for the duration of the experiment. Heart rate, body temperature, and blood oxygenation were continuously monitored throughout the experiment. A heating pad maintained body temperature between 34–36 °C throughout the experiment. At the end of the study, animals were deeply euthanized with 120 mg kg^{-1} sodium pentobarbital (MWI). Spinal cords were extracted from the T12 through L6 vertebral segments and placed in 4% PFA at 4 °C overnight. Spinal cords were then stored in saline at 4 °C.

Data Collection: Stimulation with the microelectrode array was performed using the RHS Stim/Recording controller (Intan Technologies). EMG recording was performed with the RHD Recording controller (Intan Technologies). For each experiment, stimulation was delivered to pairs of contacts in a semi-random order at a single current level. Each stimulation train consisted of 5 trials delivered at 0.5 Hz. The order of current levels was randomized. Data was captured on the RHS and RHD controllers at a sampling rate of 30 kHz/s and 20 kHz s^{-1}, respectively. During recording, data was bandpass filtered 0.09 Hz to 7.6 kHz.

Data Processing: EMG recordings were first notch filtered at 60 Hz, then bandpass filtered 10–1000 Hz using a 2nd order Butterworth filter. After filtering, data was segmented into trials (30 ms window of data) and trial averaged. Peak-to-peak amplitudes were calculated from the maximum and minimum potentials within 1.5–15 ms after stimulus as follows:

$$PTP^{M}_{norm}\,(amp) = PTP\,(amp)\,/PTP^{M}_{max}\,(amp \in Amps) \tag{2}$$

where PTP_{norm} is the normalized peak-to-peak amplitude of the EMG response for a given muscle *M*, a given electrode contact, and a given current level *amp*, *PTP* is the peak-to-peak amplitude of the EMG response for a given muscle *M*, a given electrode contact, and a given current level *amp*, and PTP^{M}_{max} is the maximum peak-to-peak amplitude for muscle *M* across all stimulation contacts and all current levels *Amps*.

Selectivity Index Calculation: Selectivity indices were calculated based on previously published literature.[37] For a given muscle *M* and a given set of current amplitudes *amps* in range *Amps*, the selectivity index for a given electrode contact was calculated as follows:

$$SI = max_{amp \in Amps} \left\{ PTP^{M}_{norm}(amp) - \frac{1}{N_M - 1} \sum_{M' \neq M} PTP^{M'}_{norm}(amp) \right\} \quad (3)$$

where *SI* is the selectivity of a given muscle and a given electrode contact, $PTP^{M}_{norm}(amp)$ is the normalized peak-to-peak amplitude of the EMG response for muscle *M* and current amplitude *amp*, and N_M is the number of muscles recorded.

Inter-Cathode Pitch Calculation from Poisson Disk Sampling: The resultant inter-cathode pitch from each subsample in the Poisson Disk sampling was calculated as follows:

$$pitch = \sqrt{\frac{x \times y}{n}} \quad (4)$$

where x and y are the length and width of the SpineWrap array and *n* is the number of bipolar contact pairs in the subsample. Note that the pitch between the cathode and anode in each pair remained constant at 360 µm.

Supporting Information

Supporting Information is available from the Wiley Online Library or from the author.

Acknowledgements

The authors acknowledge insightful discussions with Dr. Roland Lee, Chief of Neuroradiology and Professor in Radiology at UC San Diego, who advised on the MRI protocols. The authors also acknowledge recommendations from Dr. David Roth, Professor of Anesthesiology at UC San Diego, on surgical setup and anesthesia protocols. The authors are also grateful for the technical support from the nano3 cleanroom facilities at UCSD's Qualcomm Institute where the electrode fabrication was conducted. This work was performed, in part, at the San Diego Nanotechnology Infrastructure (SDNI) of UCSD, a member of the National Nanotechnology Coordinated Infrastructure, which is supported by the NSF (grant ECCS1542148). This work was primarily funded by 2 Galvanizing Engineering in Medicine (GEM) awards (S.A.D, J.C., and S.B-H.), an initiative of UC San Diego Altman Clinical and Translational Research Institute (ACTRI) and UC San Diego Institute of Engineering in Medicine (IEM). S.M.R. was funded as a UC San Diego Interfaces Graduate Training Program Fellow (National Institute of Biomedical Imaging and Bioengineering, NIBIB T32 EB009380). Investigators were supported in part by the National Institutes of Health's *Brain Research Through Advancing Innovative Neurotechnologies* Initiative, The BRAIN Initiative, awards UG3NS123723-01 (S.A.D.) and R01NS123655-01 (S.A.D.), the NIH NIBIB Director's New Innovator Award, DP2-EB029757 (S.A.D.), and Veterans Affairs Merit Award, 1I01BX005952 (E.Y.C.).

Conflict of Interest

The authors declare the following competing interests not directly related to this work: S.A.D. and S.B.H. have competing interests including equity in Cortical Science Inc. S.A.D. was a paid consultant to MaXentric Technologies.

Author Contributions

S.M.R. and S.A.D. conceived the project and designed the experiments. S.M.R. designed and fabricated the microelectrode arrays. S.M.R., R.M.W., L.D.-A., and H.S.U were involved in surgical planning and performed the in vivo data acquisition. S.M.R. analyzed the data with input from S.A.D. and T.Y. R.M.W. performed the MRI reconstruction and participated in data analysis. S.M.R. and R.V. performed the modeling simulations. E.Y.C. and Q.T. performed the MRI imaging. S.M.R. and S.A.D. wrote the paper. S.A.D., S.B.-H., and J.C. contributed to the funding acquisition. All authors discussed and contributed to the revision of the manuscript. S.A.D. supervised the project.

Data Availability Statement

All data obtained in this study is either presented in the paper and the Supplementary Materials or is available in open database. Rat spinal cord recording and stimulation data is available on DANDI. Data was acquired using Intan software (https://intantech.com/RHX_software.html) and processed via MATLAB (Mathworks, Natick, MA). Custom MATLAB code (version R2022b) is available on GitHub (https://srussman.github.io/).

Keywords

epidural electrical stimulation, microelectrode array, platinum nanorod, spinal cord stimulation, thin film

Received: October 27, 2024
Published online:

[1] C. N. Shealy, J. T. Mortimer, J. B. Reswick, *Anesth. Analg.* **1967**, *46*, 489.
[2] G. Molnar, G. Barolat, *Neuromodulation* **2014**, *17*, 12.
[3] N. Wenger, E. M. Moraud, J. Gandar, P. Musienko, M. Capogrosso, L. Baud, C. G. Le Goff, Q. Barraud, N. Pavlova, N. Dominici, I. R. Minev, L. Asboth, A. Hirsch, S. Duis, J. Kreider, A. Mortera, O. Haverbeck, S. Kraus, F. Schmitz, J. DiGiovanna, R. van den Brand, J. Bloch, P. Detemple, S. P. Lacour, E. Bézard, S. Micera, G. Courtine, *Nat. Med.* **2016**, *22*, 138.
[4] F. B. Wagner, J.-B. Mignardot, C. G. Le Goff-Mignardot, R. Demesmaeker, S. Komi, M. Capogrosso, A. Rowald, I. Seáñez, M. Caban, E. Pirondini, M. Vat, L. A. McCracken, R. Heimgartner, I. Fodor, A. Watrin, P. Seguin, E. Paoles, K. Van Den Keybus, G. Eberle, B. Schurch, E. Pralong, F. Becce, J. Prior, N. Buse, R. Buschman, E. Neufeld, N. Kuster, S. Carda, J. von Zitzewitz, V. Delattre, et al., *Nature* **2018**, *563*, 65.
[5] M. Capogrosso, T. Milekovic, D. Borton, F. Wagner, E. M. Moraud, J.-B. Mignardot, N. Buse, J. Gandar, Q. Barraud, D. Xing, E. Rey, S. Duis, Y. Jianzhong, W. K. D. Ko, Q. Li, P. Detemple, T. Denison, S. Micera, E. Bezard, J. Bloch, G. Courtine, *Nature* **2016**, *539*, 284.
[6] S. Harkema, Y. Gerasimenko, J. Hodes, J. Burdick, C. Angeli, Y. Chen, C. Ferreira, A. Willhite, E. Rejc, R. G. Grossman, V. R. Edgerton, *Lancet* **2011**, *377*, 1938.
[7] R. M. Ichiyama, Y. P. Gerasimenko, H. Zhong, R. R. Roy, V. R. Edgerton, *Neurosci. Lett.* **2005**, *383*, 339.
[8] M. L. Gill, P. J. Grahn, J. S. Calvert, M. B. Linde, I. A. Lavrov, J. A. Strommen, L. A. Beck, D. G. Sayenko, M. G. Van Straaten, D. I. Drubach, D. D. Veith, A. R. Thoreson, C. Lopez, Y. P. Gerasimenko, V. R. Edgerton, K. H. Lee, K. D. Zhao, *Nat. Med.* **2018**, *24*, 1677.
[9] C. A. Angeli, M. Boakye, R. A. Morton, J. Vogt, K. Benton, Y. Chen, C. K. Ferreira, S. J. Harkema, *N. Engl. J. Med.* **2018**, *379*, 1244.

[10] M. Murg, H. Binder, M. R. Dimitrijevic, *Spinal Cord* **2000**, *38*, 394.
[11] K. Kumar, D. L. Caraway, S. Rizvi, S. Bishop, *Neuromodulation* **2014**, *17*, 22.
[12] S. F. Lempka, P. G. Patil, *Curr. Opin. Biomed. Eng.* **2018**, *8*, 51.
[13] P. E. K. Donaldson, *Progress Biomed. Appl.* **1987**, *31*, 2.
[14] S. B. Brummer, L. S. Robblee, F. T. Hambrecht, *Ann. N. Y. Acad. Sci.* **1983**, *405*, 159.
[15] A. Petrossians, J. J. Whalen, J. D. Weiland, F. Mansfeld, *J. Electrochem. Soc.* **2011**, *158*, D269.
[16] D. R. Merrill, M. Bikson, J. G. R. Jefferys, *J. Neurosci. Methods* **2005**, *141*, 171.
[17] H. Lorach, A. Galvez, V. Spagnolo, F. Martel, S. Karakas, N. Intering, M. Vat, O. Faivre, C. Harte, S. Komi, J. Ravier, T. Collin, L. Coquoz, I. Sakr, E. Baaklini, S. D. Hernandez-Charpak, G. Dumont, R. Buschman, N. Buse, T. Denison, I. van Nes, L. Asboth, A. Watrin, L. Struber, F. Sauter-Starace, L. Langar, V. Auboiroux, S. Carda, S. Chabardes, T. Aksenova, et al., *Nature* **2023**, *618*, 126.
[18] A. Rowald, S. Komi, R. Demesmaeker, E. Baaklini, S. D. Hernandez-Charpak, E. Paoles, H. Montanaro, A. Cassara, F. Becce, B. Lloyd, T. Newton, J. Ravier, N. Kinany, M. D'Ercole, A. Paley, N. Hankov, C. Varescon, L. McCracken, M. Vat, M. Caban, A. Watrin, C. Jacquet, L. Bole-Feysot, C. Harte, H. Lorach, A. Galvez, M. Tschopp, N. Herrmann, M. Wacker, L. Geernaert, et al., *Nat. Med.* **2022**, *28*, 260.
[19] D. Bendersky, C. Yampolsky, *World Neurosurg.* **2014**, *82*, 1359.
[20] G. Taccola, S. Barber, P. J. Horner, H. A. C. Bazo, D. Sayenko, *Spinal Cord* **2020**, *58*, 1049.
[21] B. Harland, Z. Aqrawe, M. Vomero, C. Boehler, E. Cheah, B. Raos, M. Asplund, S. J. O'Carroll, D. Svirskis, *Adv. Sci.* **2022**, *9*, 2105913.
[22] P. Gad, J. Choe, M. S. Nandra, H. Zhong, R. R. Roy, Y.-C. Tai, V. R. Edgerton, *J. Neuroeng. Rehabil.* **2013**, *10*.
[23] M. S. Nandra, N. MandheerejS, I. A. Lavrov, V. R. Edgerton, Y.-C. Tai, *IEEE 24th Int. Conf. on Micro Electro Mechanical Systems*, IEEE, **2011**, pp. 1007–10, https://doi.org/10.1109/MEMSYS.2011.5734598.
[24] K. W. Meacham, R. J. Giuly, L. Guo, S. Hochman, S. P. DeWeerth, *Biomed. Microdevices* **2008**, *10*, 259.
[25] V. Giagka, A. Demosthenous, N. Donaldson, *Biomed. Microdevices* **2015**, *17*.
[26] A. Garcia-Sandoval, A. Pal, A. M. Mishra, S. Sherman, A. R. Parikh, A. Joshi-Imre, D. Arreaga-Salas, G. Gutierrez-Heredia, A. C. Duran-Martinez, J. Nathan, S. M. Hosseini, J. B. Carmel, W. Voit, *J. Neural Eng.* **2018**, *15*, 045002.
[27] I. R. Minev, P. Musienko, A. Hirsch, Q. Barraud, N. Wenger, E. M. Moraud, J. Gandar, M. Capogrosso, T. Milekovic, L. Asboth, R. F. Torres, N. Vachicouras, Q. Liu, N. Pavlova, S. Duis, A. Larmagnac, J. Vörös, S. Micera, Z. Suo, G. Courtine, S. P. Lacour, *Science* **2015**, *347*, 159.
[28] M. Ganji, A. C. Paulk, J. C. Yang, N. W. Vahidi, S. H. Lee, R. Liu, L. Hossain, E. M. Arneodo, M. Thunemann, M. Shigyo, A. Tanaka, S. B. Ryu, S. W. Lee, Y. Tchoe, M. Marsala, A. Devor, D. R. Cleary, J. R. Martin, H. Oh, V. Gilja, T. Q. Gentner, S. I. Fried, E. Halgren, S. S. Cash, S. A. Dayeh, *Nano Lett.* **2019**, *19*, 6244.
[29] R. Vatsyayan, D. Cleary, J. R. Martin, E. Halgren, S. A. Dayeh, *J. Neural Eng.* **2021**, 046077, *18*.
[30] Y. Tchoe, A. M. Bourhis, D. R. Cleary, B. Stedelin, J. Lee, K. J. Tonsfeldt, E. C. Brown, D. A. Siler, A. C. Paulk, J. C. Yang, H. Oh, Y. G. Ro, K. Lee, S. M. Russman, M. Ganji, I. Galton, S. Ben-Haim, A. M. Raslan, S. A. Dayeh, *Sci. Transl. Med.* **2022**, 1441.
[31] S. M. Russman, D. R. Cleary, Y. Tchoe, A. M. Bourhis, B. Stedelin, J. Martin, E. C. Brown, X. Zhang, A. Kawamoto, W. H. A. Ryu, A. M. Raslan, J. D. Ciacci, S. A. Dayeh, *Sci. Transl. Med.* **2022**, *14*, 4744.
[32] K. Lee, A. C. Paulk, Y. G. Ro, D. R. Cleary, K. J. Tonsfeldt, Y. Kfir, J. S. Pezaris, Y. Tchoe, J. Lee, A. M. Bourhis, R. Vatsyayan, J. R. Martin, S. M. Russman, J. C. Yang, A. Baohan, R. M. Richardson, Z. M. Williams, S. I. Fried, U. Hoi Sang, A. M. Raslan, S. Ben-Haim, E. Halgren, S. S. Cash, S. A. Dayeh, *Nat. Commun.* **2024**, *15*, 046030.
[33] J. Holsheimer, W. A. Wesselink, *Med. Biol. Eng. Comput.* **1997**, *35*, 493.
[34] M. Capogrosso, N. Wenger, S. Raspopovic, P. Musienko, J. Beauparlant, L. Bassi Luciani, G. Courtine, S. Micera, *J. Neurosci.* **2013**, *33*, 19326.
[35] C. C. Mcintyre, W. M. Grill, *J. Neurophysiol.* **2002**, *88*, 1592.
[36] I. Uguz, K. L. Shepard, *Sci. Adv.* **2022**, *8*, eabq6354.
[37] N. Greiner, B. Barra, G. Schiavone, N. James, F. Fallegger, S. Borgognon, S. Lacour, J. Bloch, G. Courtine, M. Capogrosso, *Nat. Commun.* **2020**, *12*, 435.
[38] C. W. Chang, Y. K. Lo, P. Gad, R. Edgerton, W. Liu, *36th Annual Int. Conf. of the IEEE Engineering in Medicine and Biology Society*, IEEE, **2014**, pp. 6834–7, https://ieeexplore.ieee.org/document/6945198.
[39] E. J. Peterson, O. Izad, D. J. Tyler, *J. Neural Eng.* **2011**, *8*.
[40] V. R. Edgerton, G. Courtine, Y. P. Gerasimenko, I. Lavrov, R. M. Ichiyama, A. J. Fong, L. L. Cai, C. K. Otoshi, N. J. K. Tillakaratne, J. W. Burdick, R. R. Roy, *Brain Res. Rev.* **2008**, *57*, 241.
[41] Y. P. Gerasimenko, I. A. Lavrov, G. Courtine, R. M. Ichiyama, C. J. Dy, H. Zhong, R. R. Roy, V. R. Edgerton, *J. Neurosci. Methods* **2006**, *157*, 253.
[42] A. Toossi, B. Bergin, M. Marefatallah, B. Parhizi, N. Tyreman, D. G. Everaert, S. Rezaei, P. Seres, J. C. Gatenby, S. I. Perlmutter, V. K. Mushahwar, *Sci. Rep.* **2021**, *11*.
[43] R. V. Haberberger, C. Barry, N. Dominguez, D. Matusica, *Front. Cell Neurosci.* **2019**, *13*.
[44] J.-Y. Hong, S.-W. Suh, S.-Y. Park, H. N. Modi, I. J. Rhyu, S. Kwon, H. Yu, J. Byun, *Spine J.* **2011**, *11*, 1121.
[45] J. T. Maikos, Z. Qian, D. Metaxas, D. I. Shreiber, *J. Neurotrauma* **2008**, *25*, 795.
[46] J. A. Hokanson, R. A. Gaunt, D. J. Weber, *Sci. Rep.* **2018**, *8*.
[47] D. G. Sayenko, C. Angeli, S. J. Harkema, V. Reggie Edgerton, Y. P. Gerasimenko, *J. Neuro-Physiol.* **2014**, *111*, 1088.
[48] P. K. Shah, S. Sureddi, M. Alam, H. Zhong, R. R. Roy, V. R. Edgerton, Y. Gerasimenko, *J. Neurotrauma* **2016**, *33*, 1709.
[49] F. Dose, R. Deumens, P. Forget, G. Taccola, *Spinal Cord* **2016**, *54*, 93.
[50] D. G. Sayenko, D. A. Atkinson, T. C. Floyd, R. M. Gorodnichev, T. R. Moshonkina, S. J. Harkema, V. R. Edgerton, Y. P. Gerasimenko, *Neurosci. Lett.* **2015**, *609*, 229.
[51] M. P. Côté, M. Murray, M. A. Lemay, *J. Neurotrauma* **2017**, *34*, 1841.

Supplementary Materials

This file includes:

Figures S1 to S16

Tables S1 to S3

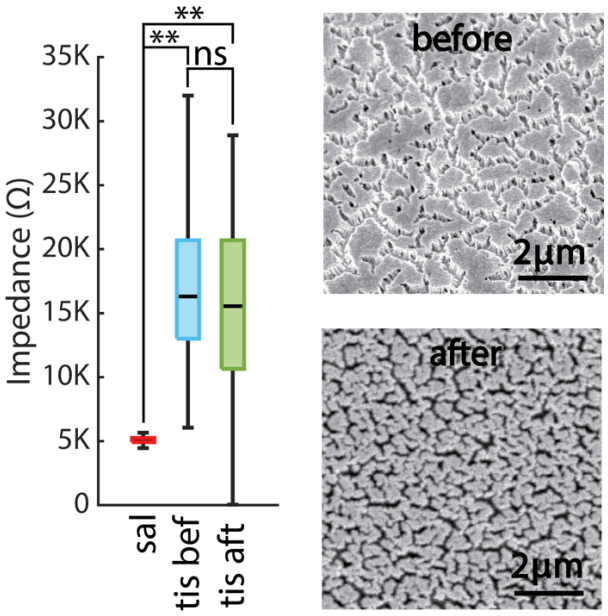

Figure S1. PtNRs were stable during the acute stimulation study. Left: SpineWrap average impedances measured at three timepoints during experiment: in saline before implantation, *in vivo* before stimulation, and *in vivo* after experiment completion. Right: SEM images before and after stimulation showed no morphological changes to PtNR structure.

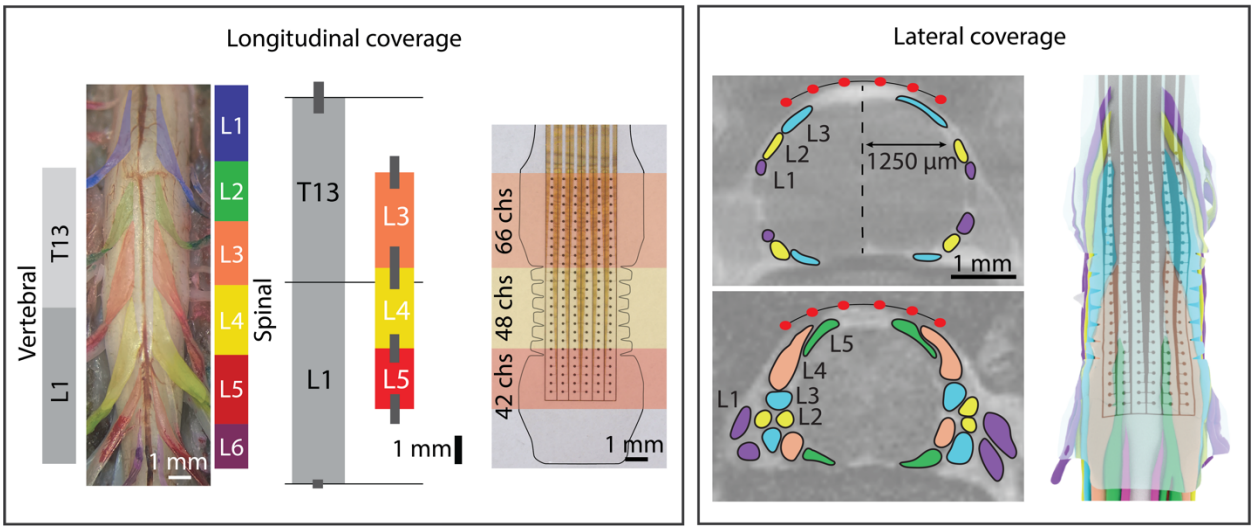

Figure S2. SpineWrap dimensions are tailored to the L3-L5 DREZs. Longitudinal coverage: Dissection of L1 through L6 DRs and their DREZs allowed for determination of optimal longitudinal contact pitch and electrode length. The mean T13-L1 vertebral and L3-L5 spinal segment lengths are shown (n = 5). Gray vertical bars indicate +/- 1 standard deviation. Lateral coverage: Cross-sectional MRI scans identified the lateral spread of the DREZs and allowed for determination of optimal lateral contact pitch and electrode width.

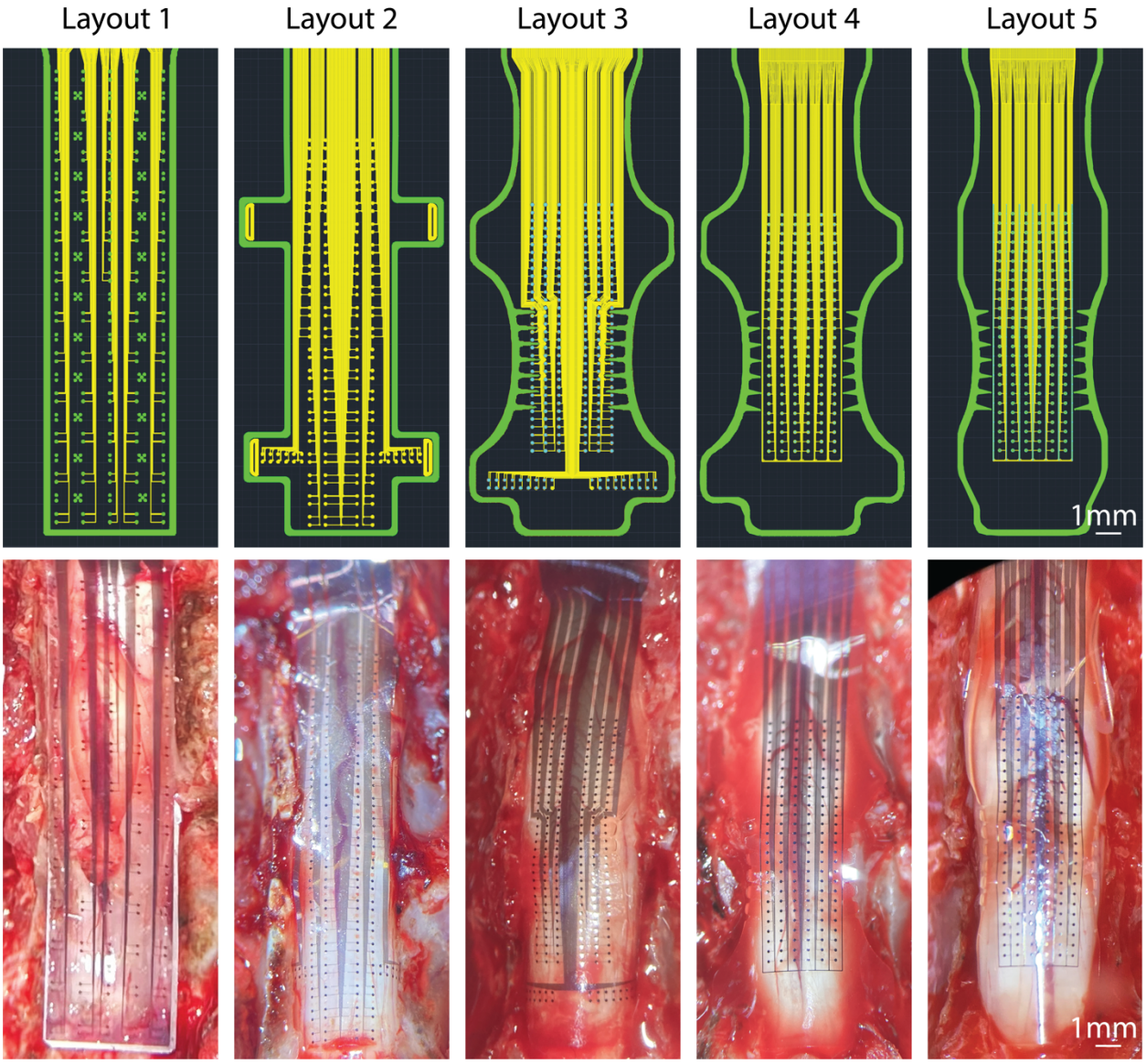

Figure S3. Electrode design iterations. Each of the five electrode iterations are shown. Top: Electrode layout in AutoCAD. Metal leads are in yellow and vias for PtNR contacts and for perfusion (only left most) are in green. Bottom: Images of the corresponding electrodes on the spinal cord.

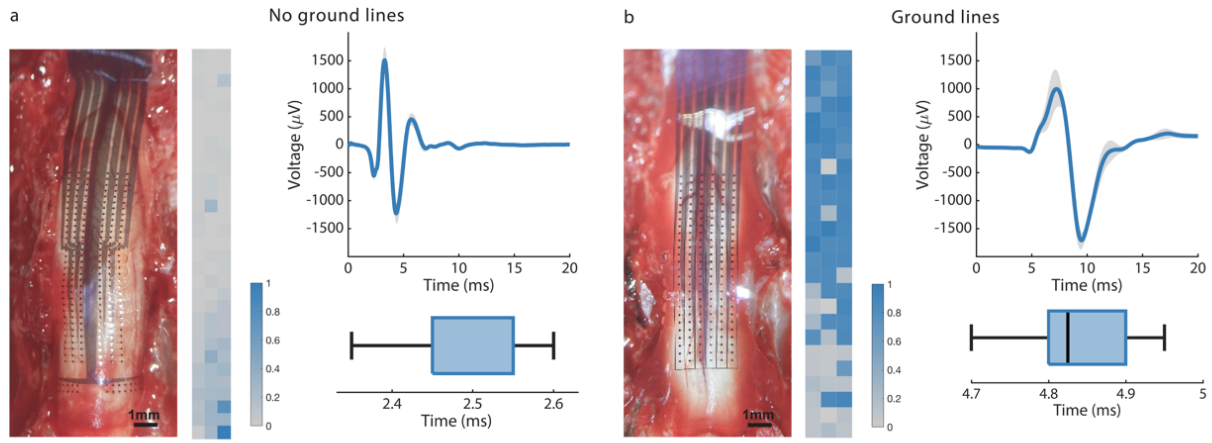

Figure S4. On-device ground limits current spread during stimulation. (a) Left: Electrode design without on-device ground and example peak-to-peak amplitude response heatmap for 150 µA stimulation current. Right: An example response and the median response latency. The boxplot shows the distribution of the current threshold for a given dataset and muscle. The horizontal center lines and boxes indicate the median and the 25th/75th percentile and the vertical solid lines represent the full range of the distribution. (b) Left: Electrode design with on-device ground and example peak-to-peak amplitude response heatmap for 150 µA stimulation current. Right: An example response and the median response latency. The boxplot shows the distribution of the current threshold for a given dataset and muscle. The horizontal center lines and boxes indicate the median and the 25th/75th percentile and the vertical solid lines represent the full range of the distribution.

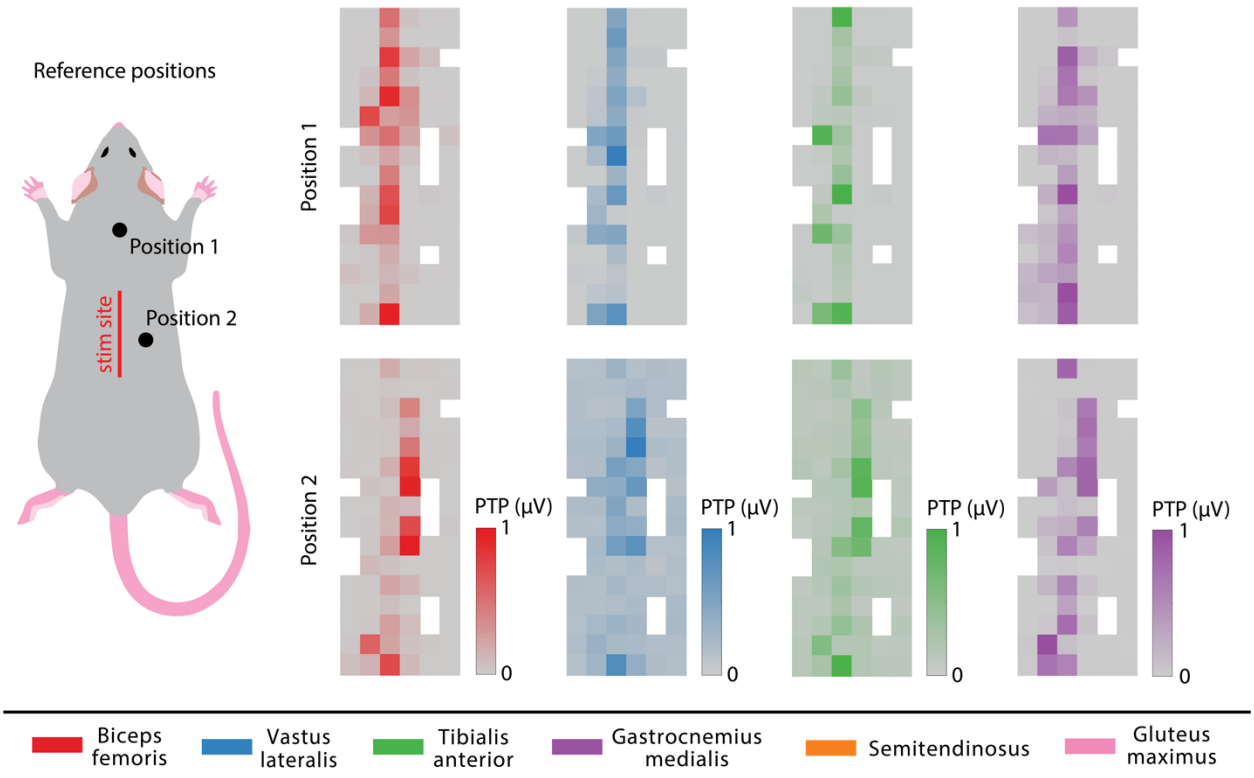

Figure S5. Shift in stimulation hotspots with ground placement in electrode without on-device ground in a single electrode placement on one rat's spinal cord. When ground needle was moved from position 1 to position 2, the locations where stimulation resulted in muscle activity shifted towards position 2.

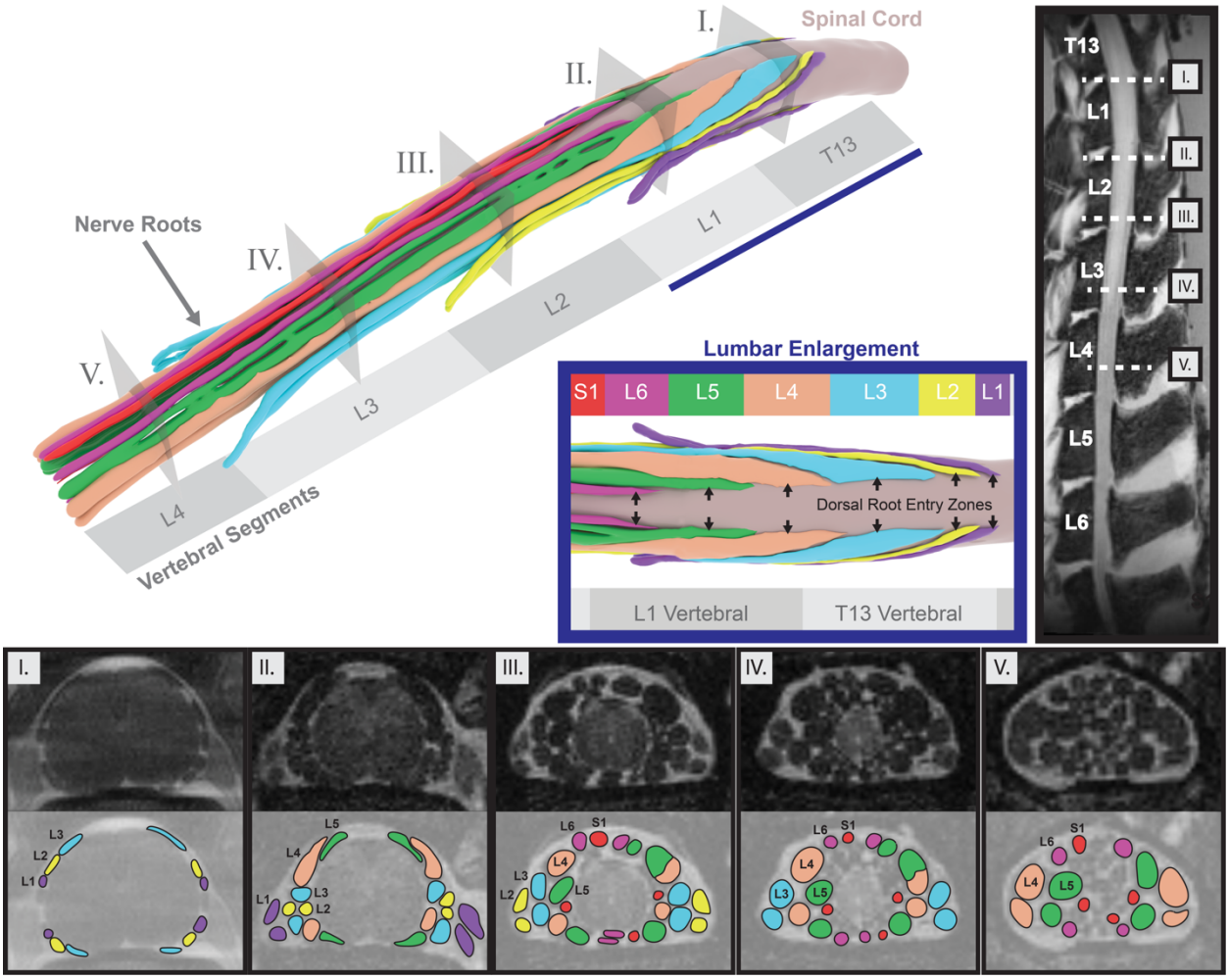

Figure S6. 3D reconstruction of nerve roots in the lumbosacral rat spinal cord. The spinal cord and nerve roots were reconstructed between the T13 - L4 vertebral segments using coronal views of the lumbar enlargement. The resulting reconstruction was used for electrode layout considerations and computational modeling.

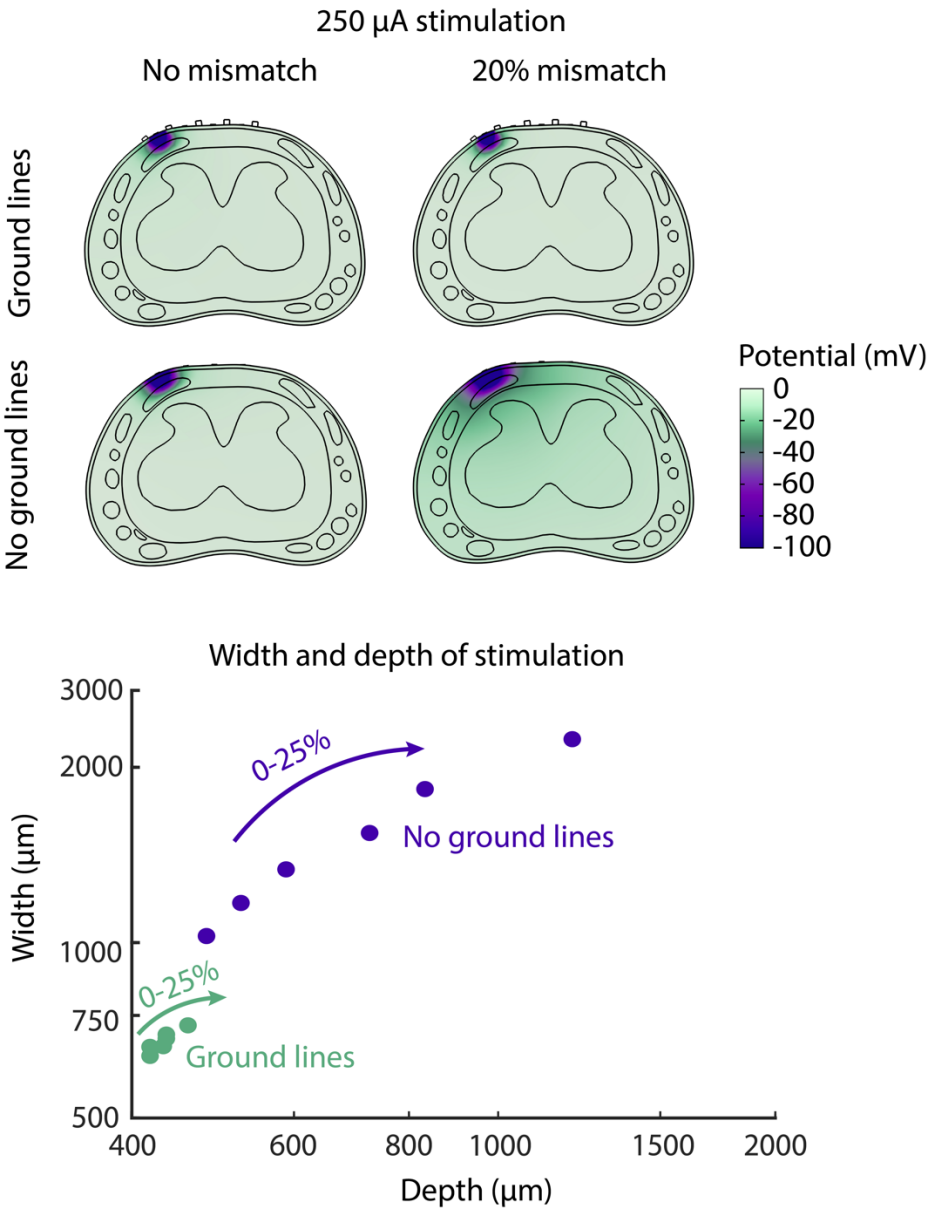

Figure S7. Modeling stimulation focality during charge mismatch. Top: The resulting potential gradients during 250 µA bipolar stimulation were evaluated for electrode arrays with and without on-device ground. Potential gradients were computed for a bipolar stimulation that is perfectly matched (left) and with 20% charge mismatch (right). Bottom: Impact of % mismatch on width and depth of stimulation at 250 µA for the electrode arrays with and without on-device ground.

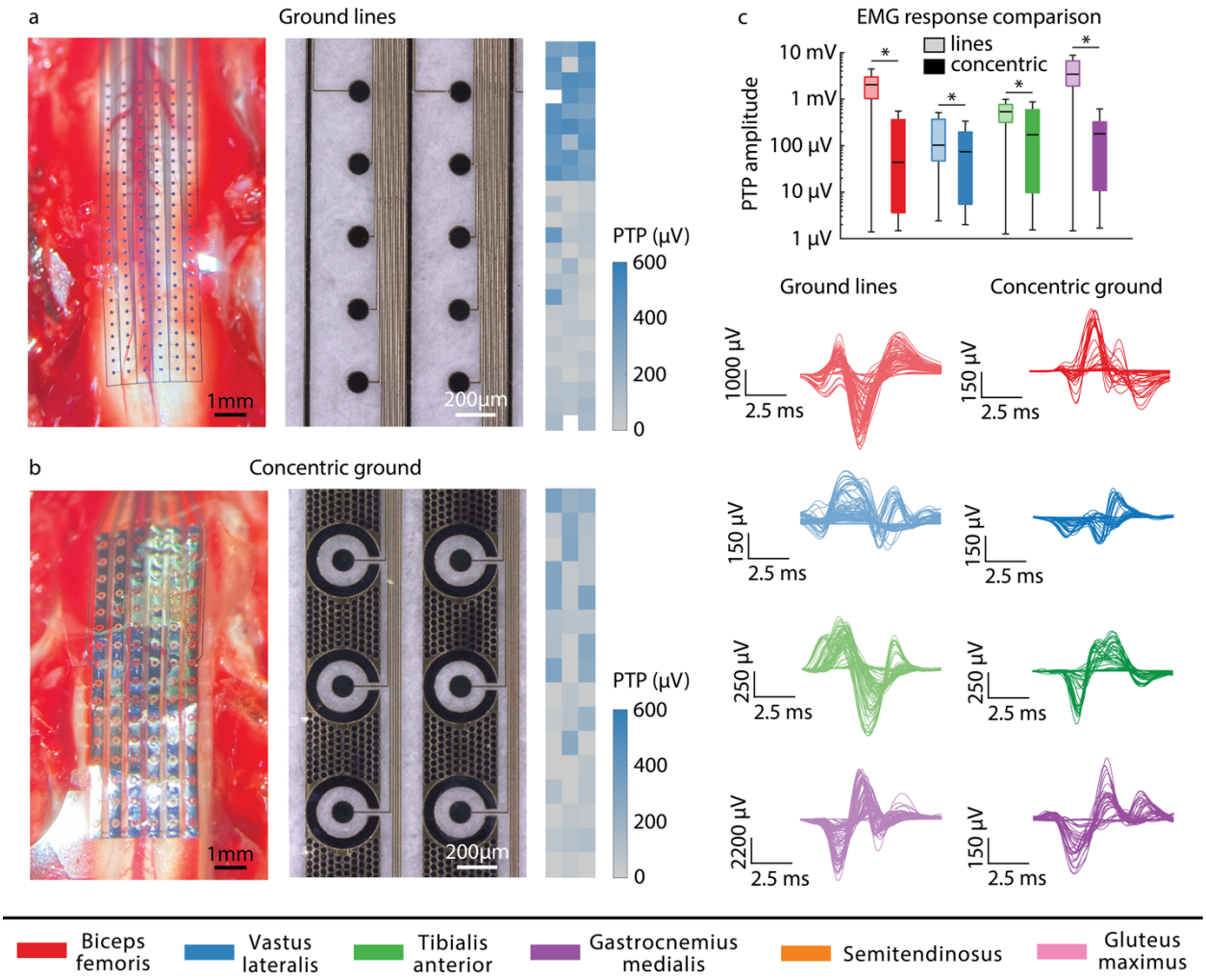

Figure S8. Comparison of on-device ground lines versus concentric ground. a Left: An example electrode with on-device ground lines. Middle: Microscope image of contacts and ground lines. Right: Heatmap of PTP amplitudes of the VAS muscle at 250 µA stimulation. b Left: An example electrode with on-device concentric ground. Middle: Microscope image of contacts and ground rings. Right: Heatmap of PTP amplitudes of the VAS muscle at 250 µA stimulation. c Comparison of PTP amplitudes to 250 µA stimulation for both ground configurations. The electrode with ground lines produced consistently higher muscle responses across all muscles measured.

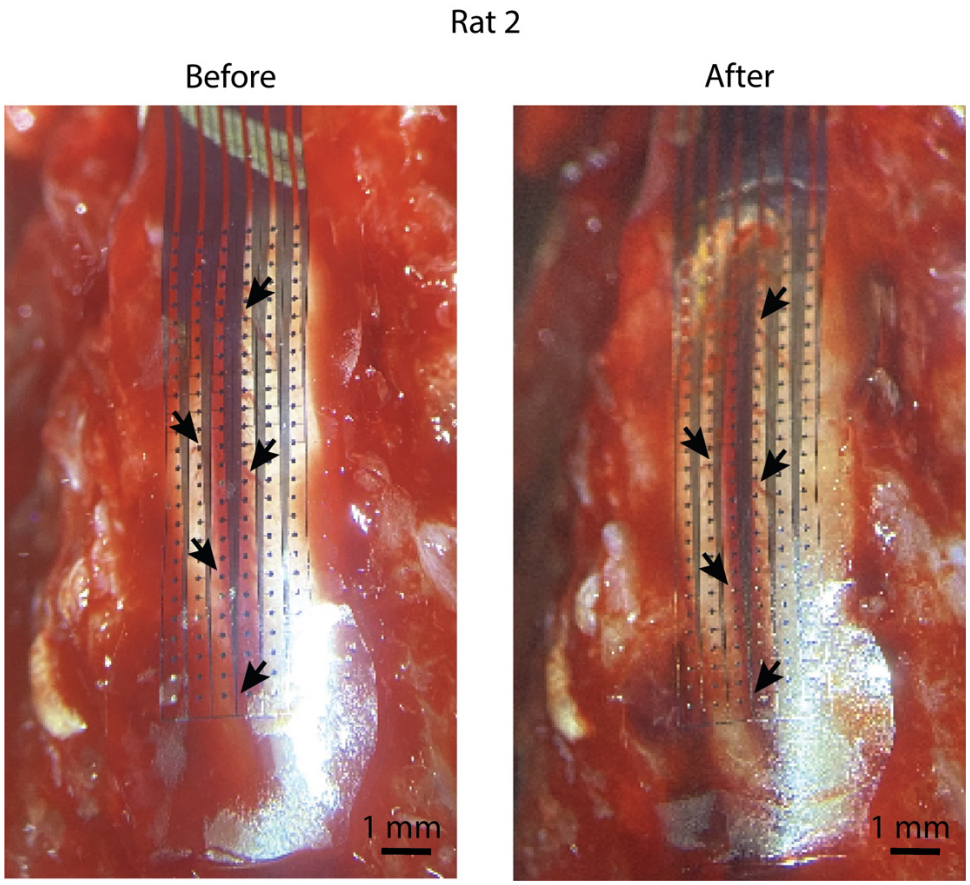

Figure S9. Electrode placement remained consistent during stimulation. Black arrows highlight vasculature used to determine relative placement before and after stimulation.

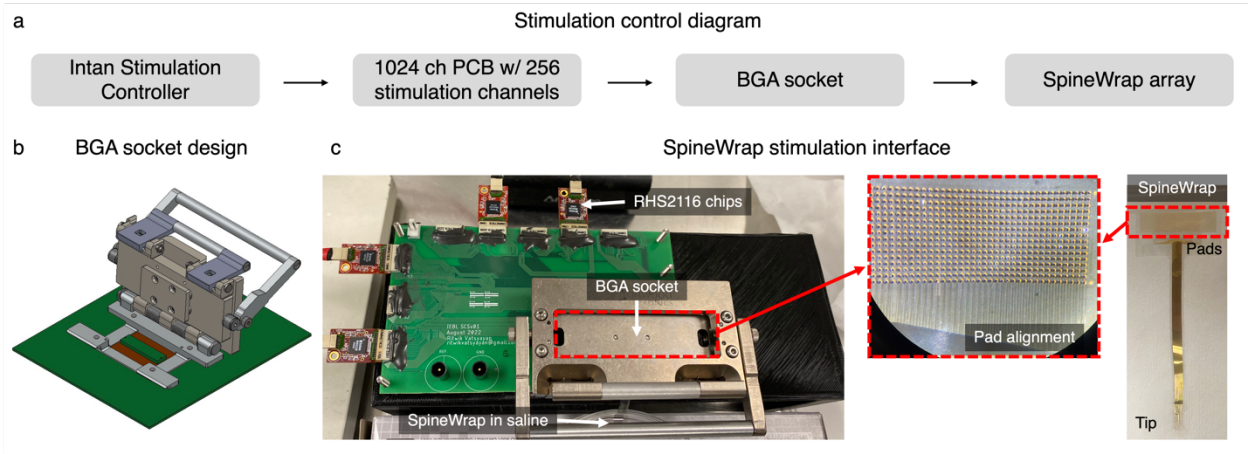

Figure S10. SpineWrap stimulation setup. (a) Stimulation was delivered via the Intan RHS Stim/Recording System and a custom-designed PCB. (b) The PCB was equipped with a BGA socket and clamshell lid. (c) The SpineWrap connector region was aligned face-down to BGA socket under a microscope. The electrode tip containing the electrode array contacts came off the bottom of the PCB to interface with the spinal cord. The BGA socket was designed for versatile use and contained 1024 recording-only, 256 stimulation/recording positions, and ground/reference positions. The recording-only positions were not used in this study.

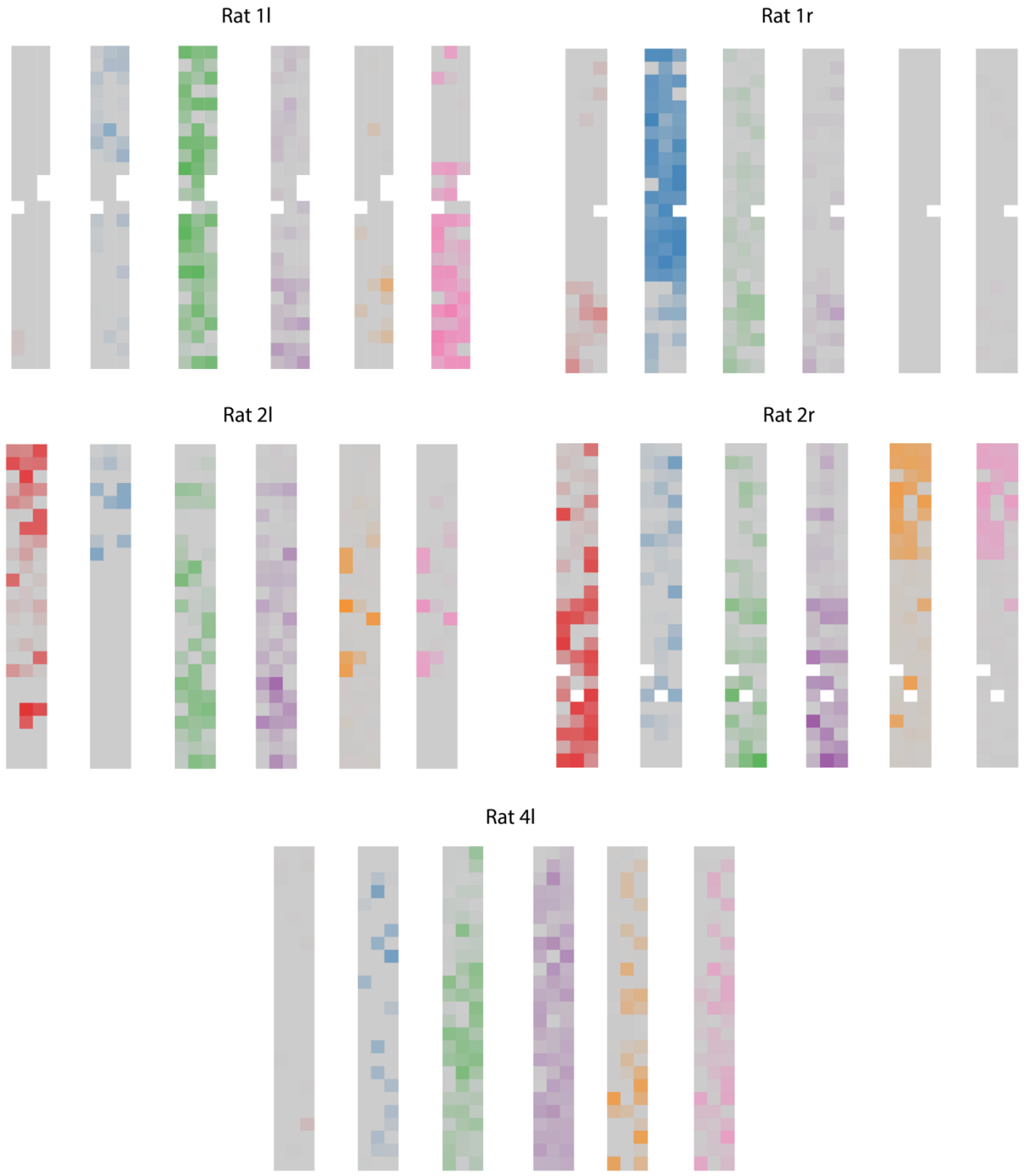

Figure S11. Selectivity index distribution across all datasets. The segmental locations of highly selective channels were consistent across animals with a few exceptions, such as the BIC in Rat 2l and the SEM and GLU in rat 2r, which were selective in the upper part of the array.

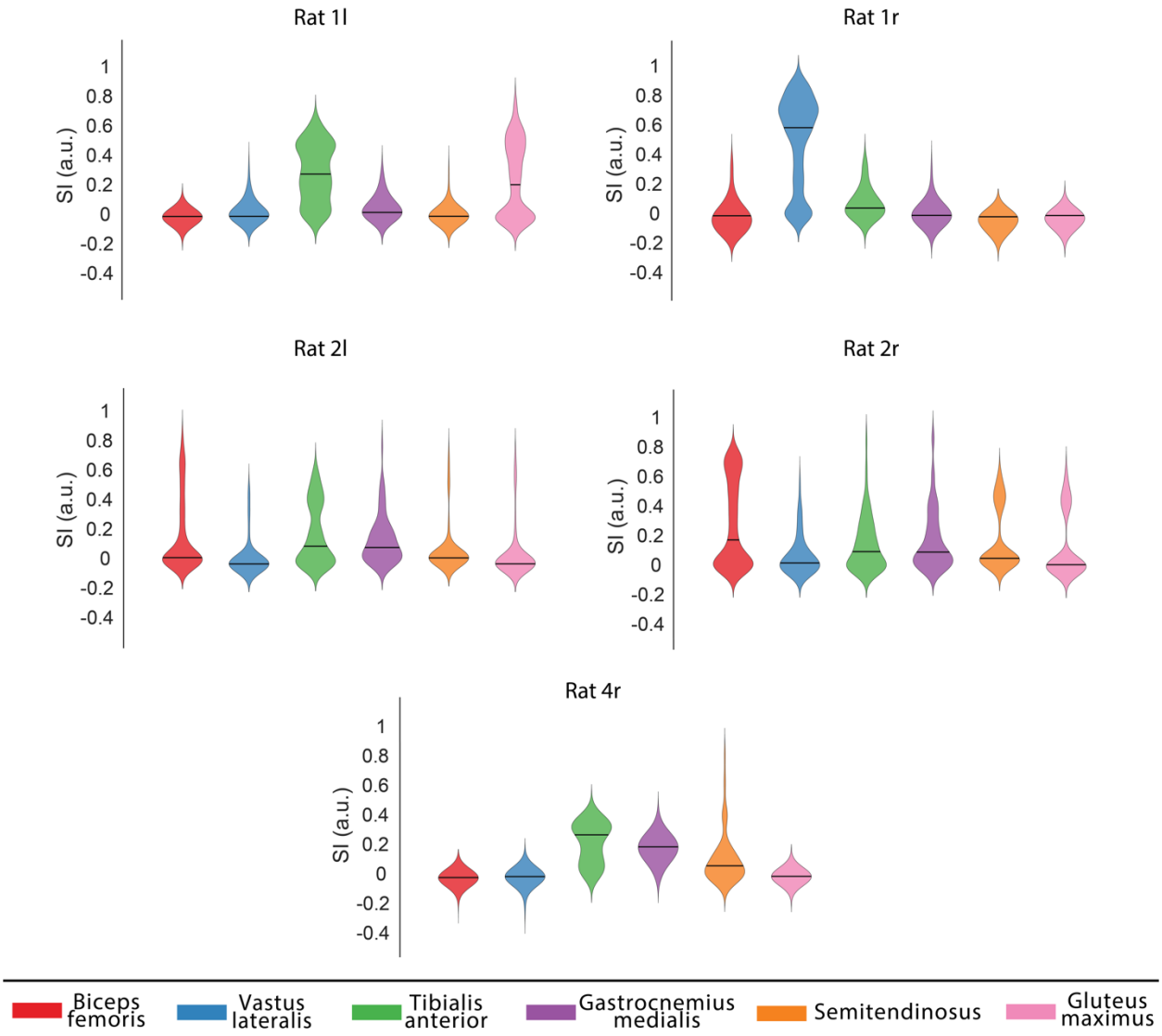

Figure S12. Selectivity index distribution per dataset. The SI distribution per muscle skewed towards low SI values.

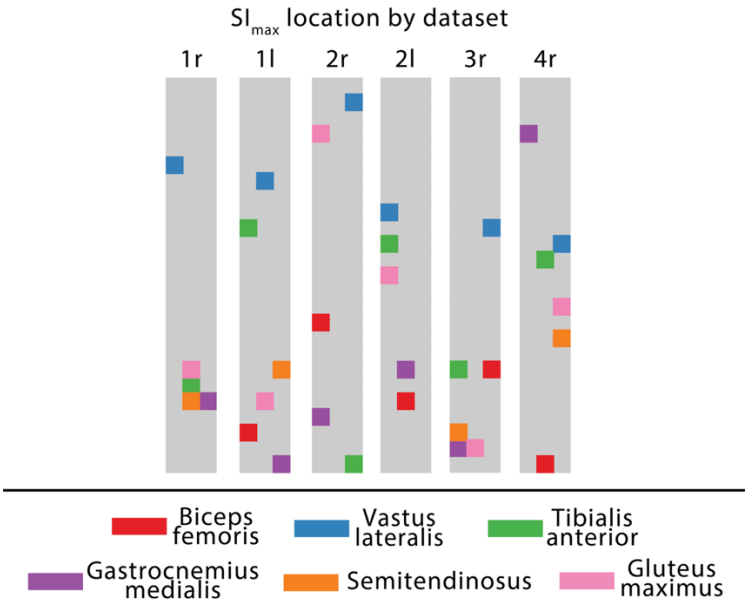

Figure S13. Locations of most selective channels by muscle for each dataset.

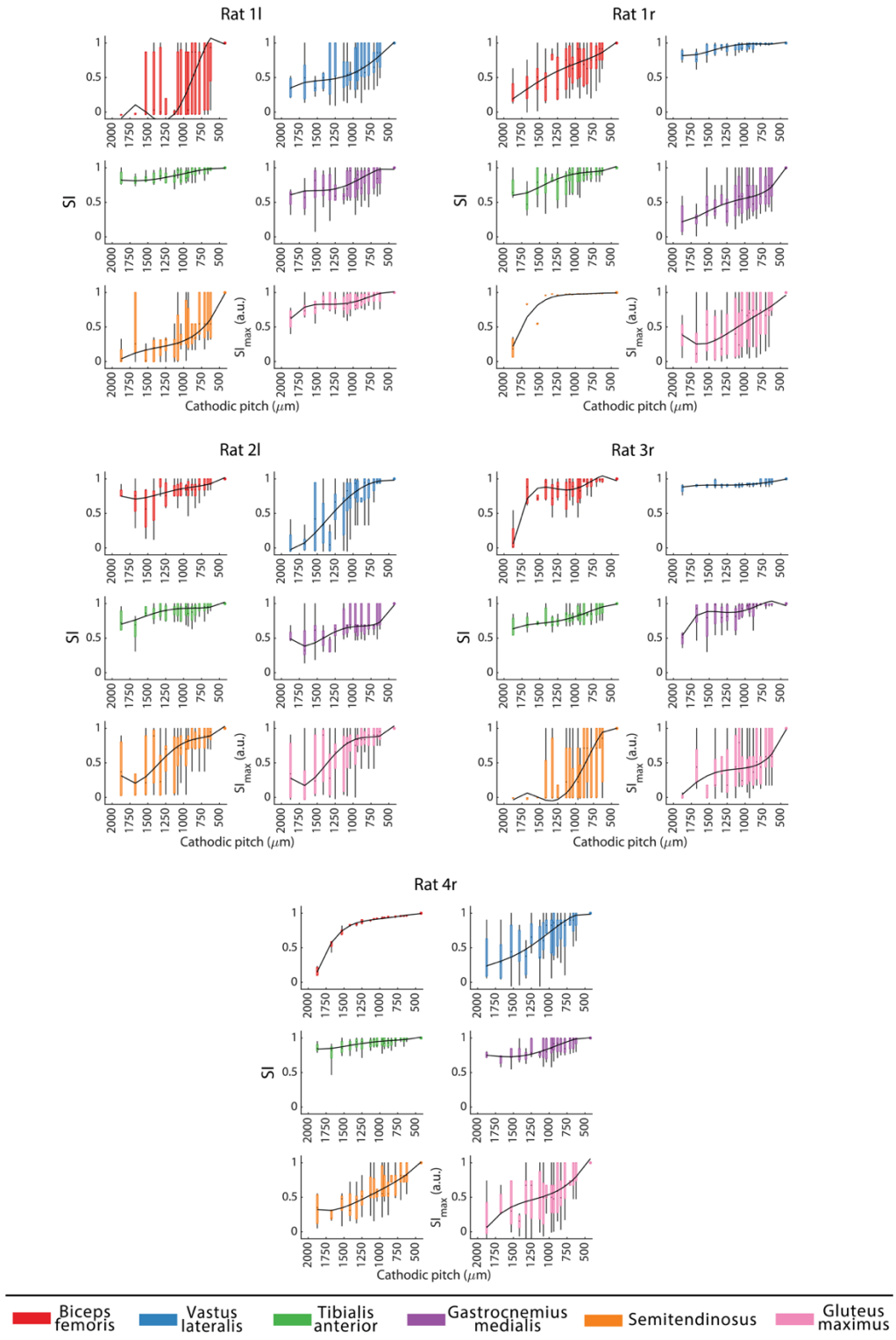

Figure S14. Maximum selectivity for subsamples across datasets. The maximum selectivity increases with decreasing pitch (increasing density) of the array. The horizontal center lines and boxes indicate the median and the 25th/75th percentile and the vertical solid lines represent the full range of the distribution. Note that at 100% there is only one datapoint, which is the SI_{max} of the full array.

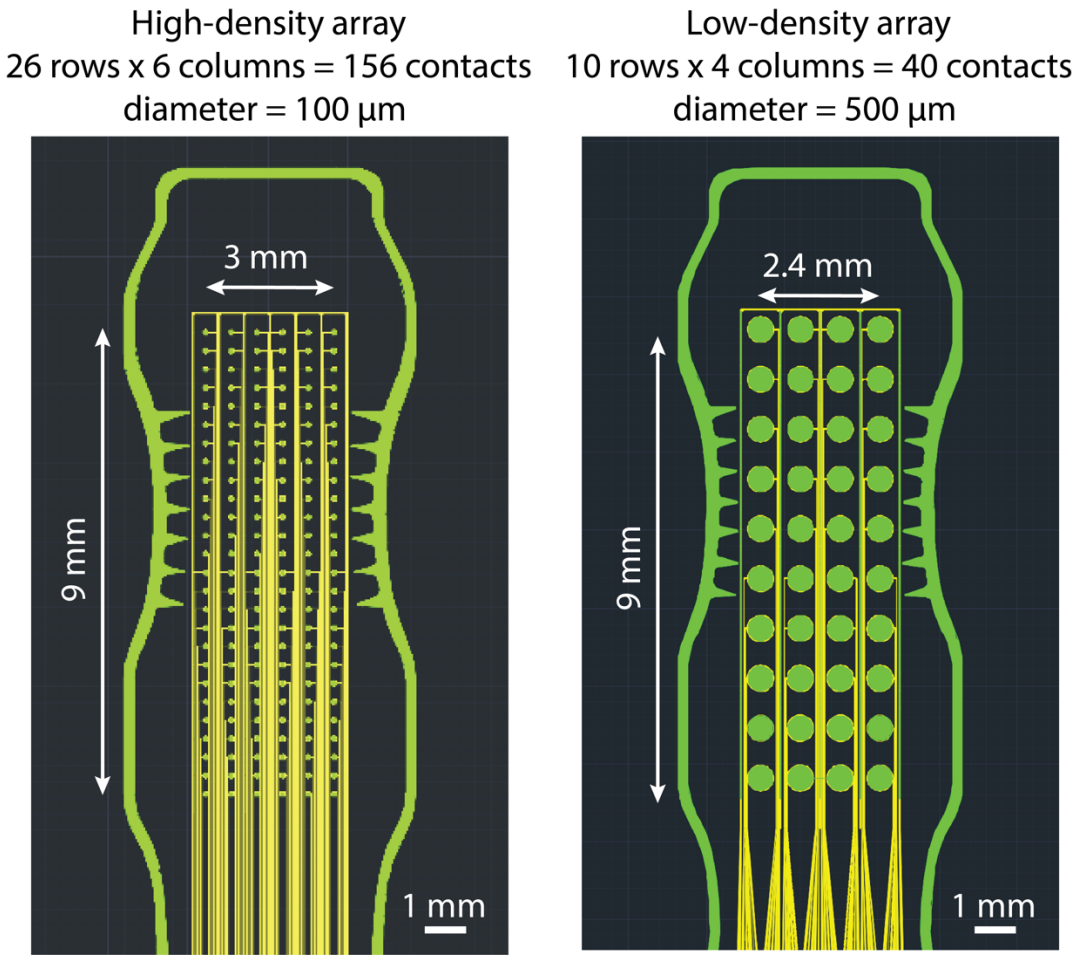

Figure S15. Comparison of design of high-density SpineWrap array and the low-density array. The horizontal and vertical pitch of the contacts increased from 500 µm and 360 µm to 1000 µm and 800 µm, respectively. The resulting channel count of the low-density array was reduced from 156 contacts to 40 contacts and the resulting density dropped from 5.6 contacts/mm^2 to 1.42 contacts/mm^2.

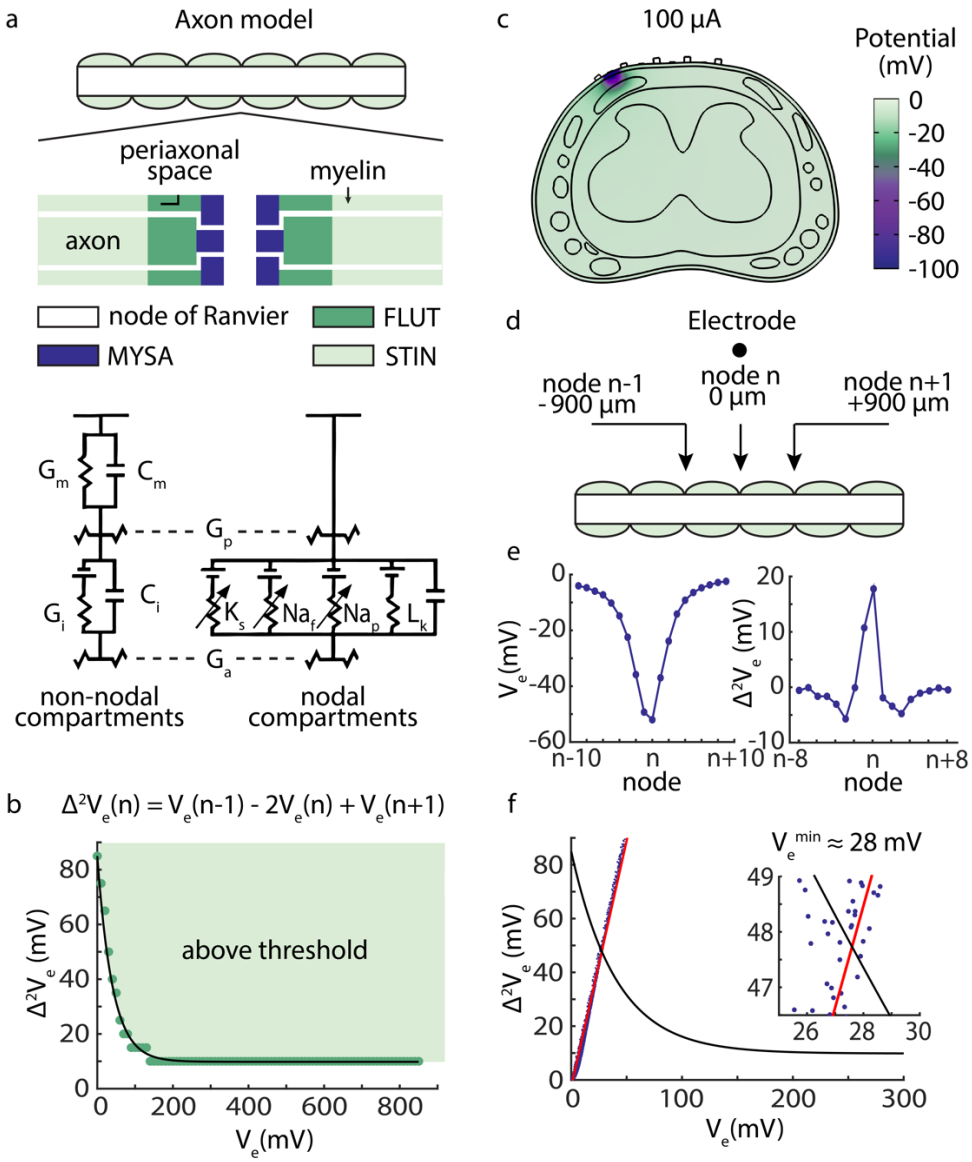

Figure S16. Determination of activation threshold. a The axon model used by Peterson et al. for evaluating the effect of the extracellular potential field on neural activation. b The single node approximation evaluated by Peterson et al. [1] The green points are taken from Petersen et al. and represent the threshold data. The black line is an exponential fit to the data. V_e is the extracellular potential at the node below the electrode and Δ^2V_e is the second spatial difference of the extracellular potential. c The potential gradient during 100 µA unipolar, cathodic epidural stimulation with a 100 µm diameter contact. d The central node was assumed to be in the x,y plane of the stimulation electrode. The neighboring nodes were located -900 µm and +900 µm from the central node in the z-direction. e The extracellular potential and the second spatial difference of the extracellular potential due to the stimulation. Node n is the node below the electrode. f Determination of the threshold potential V_e^{min}. The blue points are all the extracellular potentials in the x,y plane and the resulting Δ^2V_e. The red line is the 2nd degree polynomial fit. The threshold was calculated as the intersection point between the threshold curve and the polynomial fit.

Table S1. Vertebral and spinal segment lengths determined through dissection.

	Segment Name	**Mean** ($\bar{X}$)	**Standard Deviation** (s)
Vertebral Segment Length	T13	6.60mm	0.57mm
	L1	7.30mm	0.14mm
Spinal Segment Length	L3	3.28mm	0.67mm
	L4	2.73mm	0.44mm
	L5	2.40mm	0.40mm

Table S2. Volume conductor model parameters. Conductivity values were taken from Capogrosso et al.

Tissue	Conductivity (S/m)
White matter	0.6 longitudinal, 0.083 axial
Gray matter	0.23
Epidural fat	0.04
CSF	1.7
Saline	2

Table S3. Parameters for width versus depth analysis.

Radius (µm)	Cathode-anode pitch (µm) 10 x Radius	Cathode-ground pitch (µm) 5 x Radius	Current amplitude (µA)
50	500	250	50
50	500	250	60
50	500	250	70
50	500	250	80
50	500	250	90
50	500	250	100
50	500	250	125
50	500	250	150
100	1000	500	30
100	1000	500	50
100	1000	500	60
100	1000	500	70
100	1000	500	80
100	1000	500	90
100	1000	500	100